Polymers for Advanced Technologies

WILEY

RESEARCH ARTICLE

Design, Synthesis, and Anticancer Evaluation of a Limonene-Based LIM-*co*-NCA Copolymer via Experimental and Computational Approaches

Hülya Elmali Gülbaş[1] | Nevin Çankaya[2] | Tuncay Karakurt[3] | Murat Misir[3] | Serap Yalçin Azarkan[4]

[1]Department of Chemistry and Chemical Processing Technologies, Banaz Vocational School, Usak University, Usak, Turkey | [2]Department of Oral and Dental Health, Vocational School of Health Services, Usak University, Usak, Turkey | [3]Department of Chemical and Process Engineering, Faculty of Engineering-Architecture, Kırsehir Ahi Evran University, Kırsehir, Turkey | [4]Department of Medical Pharmacology, Kırsehir Ahi Evran University, Faculty of Medicine, Kırşehir, Turkey

Correspondence: Hülya Elmali Gülbaş (hulya.elmali@usak.edu.tr)

Received: 7 July 2025 | **Revised:** 19 September 2025 | **Accepted:** 27 September 2025

Keywords: antiproliferative effect | density functional theory (DFT) | he-La cell | LIM-*co*-NCA | MMPBSA | molecular dynamics (MD)

ABSTRACT

In this study, a novel copolymer of limonene and *N*-cyclohexylacrylamide (LIM-*co*-NCA) was synthesized and extensively characterized for both its physicochemical and biological properties. The chemical structure of the copolymer was confirmed through Fourier transform infrared and proton nuclear magnetic resonance spectroscopic techniques. Gel Permeation Chromatography (GPC) analysis revealed that LIM-*co*-NCA possesses low molecular weight and oligomeric characteristics. Thermal stability was evaluated using thermogravimetric analysis, while its antiproliferative potential was assessed against the HeLa cervical cancer cell line, demonstrating inhibitory effects. This study investigates the stability and binding affinities of Comp1, Comp2, and Comp3 ligands with 3FAA and 6GUB receptors using computational chemistry methods. Ligand geometries were optimized by density functional theory, and molecular dynamics simulations of 100 ns were performed with GROMACS to evaluate the conformational stability of ligand–receptor complexes. Binding free energies were calculated using the Molecular Mechanics Poisson–Boltzmann surface area approach, including per–residue decomposition to identify critical stabilizing residues. The results demonstrated a receptor–dependent binding preference: Comp2 achieved the strongest stabilization in 3FAA, supported by balanced electrostatic and hydrophobic interactions, while Comp3 dominated in 6GUB, forming a dense arginine-rich hydrogen bond network and highly favorable electrostatic interactions. Comp1, with its compact scaffold and limited hydrogen bonding capacity, consistently showed moderate binding strength, performing better in 3FAA than in 6GUB. These findings provide valuable insights into receptor-specific binding mechanisms and highlight the importance of optimizing both electrostatic and hydrophobic contributions in ligand design.

1 | Introduction

The potential uses of natural products and their derivatives in the pharmaceutical and biomedical industries have drawn more attention in recent years. Citrus oils contain limonene, a naturally occurring monocyclic terpene that has garnered a lot of attention because of its low toxicity, biocompatibility, and proven antibacterial and anticancer qualities [1]. There are encouraging opportunities to create bioactive materials with improved physicochemical and biological properties by copolymerizing new limonene-based copolymers with functional monomers [2, 3].

Because of their wide range of biological activity, structural variety, and biocompatibility, natural products and their derivatives have garnered a lot of attention lately for possible applications in the biomedical and pharmaceutical sectors [4]. Limonene, a naturally occurring monocyclic monoterpene hydrocarbon, is abundant in citrus oils, especially those made from the peels of oranges and lemons. Due to its well-established antibacterial, antifungal, antioxidant, and anticancer characteristics, as well as its low toxicity and exceptional biocompatibility, limonene has drawn attention [1, 2, 5, 6].

Through processes involving oxidative stress and modification of important signaling pathways, recent research has shown that limonene and its oxygenated derivatives can cause apoptosis and stop the growth of cancer cell lines [7]. Because of these characteristics, limonene is a desirable substrate for creating functional biomaterials.

There are encouraging prospects to create new materials with improved mechanical strength, thermal stability, solubility, and biological functionality through the copolymerization of limonene-based monomers with synthetic or bioactive functional monomers [2, 8]. For example, adding acrylamide derivatives to copolymers based on limonene can result in amphiphilic and bioactive networks that can be used for antimicrobial coatings, scaffolds for tissue engineering, and controlled drug release.

Furthermore, because limonene-derived polymers may encapsulate hydrophobic medicines and enable sustained release while reducing systemic toxicity, they are being investigated for use in drug delivery systems [9, 10]. In this regard, the creation of LIM-*co*-NCA copolymers and their oligomeric forms shows potential for specific biomedical uses, especially when in silico methods like dynamic simulations and molecular docking are used to support their stability and molecular interactions.

In this context, *N*-cyclohexylacrylamide (NCA), an amide-derived monomer, serves as a suitable comonomer for copolymerization with limonene due to its chemical reactivity and potential for forming hydrogen bonds. In the present study, a new limonene-based copolymer (LIM-*co*-NCA) was successfully synthesized and subjected to detailed structural and physicochemical characterization. Classical spectroscopic techniques, including Fourier Transform Infrared (FT-IR) and Proton Nuclear Magnetic Resonance (^{1}H-NMR) spectroscopy, were employed to confirm the chemical structure of the copolymer. Gel Permeation Chromatography (GPC) revealed an oligomeric nature with a weight average molecular weight (Mw) of 3328 and a number average molecular weight (Mn) of 2362. Thermogravimetric analysis (TGA) was utilized to evaluate the thermal stability of the copolymer. Furthermore, the antiproliferative activity of LIM-*co*-NCA was assessed against the HeLa cervical cancer cell line to explore its potential biomedical application.

Computational approaches have become indispensable in molecular modeling and drug design, offering atomistic insights into biomolecular interactions that are difficult to capture experimentally. *In silico* methods such as density functional theory (DFT) and molecular dynamics (MD) simulations enable researchers to investigate molecular structures, conformational dynamics, and interaction patterns under physiologically relevant conditions, thereby complementing and guiding experimental efforts.

In the present study, we evaluate three candidate ligands—Comp1, Comp2, and Comp3—in complex with two distinct protein receptors, 3FAA and 6GUB. A multi-level computational workflow was employed, including ligand geometry optimization via DFT, molecular docking, long-timescale MD simulations, and Molecular Mechanics Poisson-Boltzmann Surface Area (MMPBSA) free energy calculations with per-residue decomposition. By integrating structural dynamics with energetic analyses, this work aims to uncover receptor-specific binding preferences and identify the key interactions governing stability.

Our findings demonstrate that ligand performance is not uniform across receptors but highly dependent on the binding environment. Comp2 emerges as the most stable ligand in the 3FAA receptor due to balanced electrostatic and hydrophobic contributions, whereas Comp3 dominates in the 6GUB receptor through an extensive hydrogen–bond network and strong electrostatic stabilization. Comp1, with its compact structure and limited hydrogen–bonding capacity, shows moderate binding performance, more favorable in 3FAA than in 6GUB. These results highlight the importance of receptor context in evaluating ligand affinity and provide insights that may inform rational drug design strategies.

2 | Materials and Methods

All chemicals and solvents were purchased from commercial sources. Cyclohexylamine, trimethylamine, acryloyl chloride, D-limonene, and benzoyl peroxide were purchased from Aldrich Chemical Reagent Co. Ltd. 1,4-Dioxane was purchased from Merck Chemical Reagent Co. Ltd. All the solid chemicals were used as received without further purification, but before using, all solvents were distilled under vacuum.

2.1 | Measurements

Fourier transform infrared (FT-IR) studies were performed by Two (UATR) equipment using Perkin-Elmer FT-IR spectroscope. The scanned wavenumbers range from 4000 to 400 cm^{-1}. ^{1}H-NMR measurements were conducted on Bruker 400 MHz in $CDCl_3$ as solvent with tetramethylsilane (TMS) as the internal reference. The molecular weight of the LIM-*co*-NCA was determined by using gel permeation chromatography (GPC) on Waters 996 apparatus equipped with Evaporative Mass Detector, $CHCl_3$ solvent with polystyrene standards. Thermal analysis of the LIM-*co*-NCA was obtained with a Hitachi 7000 TGA/DTG (Thermogravimetric Analysis/Derivative Thermal Gravimetric Analysis) simultaneous system at a heating rate of 10°C min^{-1} in nitrogen atmosphere, from 40°C to 550°C temperatures.

2.2 | Synthesis of LIM-*co*-NCA

In the presence of cyclohexylamine, trimethylamine, and acryloyl chloride, NCA monomer was synthesized in our laboratory and characterized [11, 12]. The two appropriate

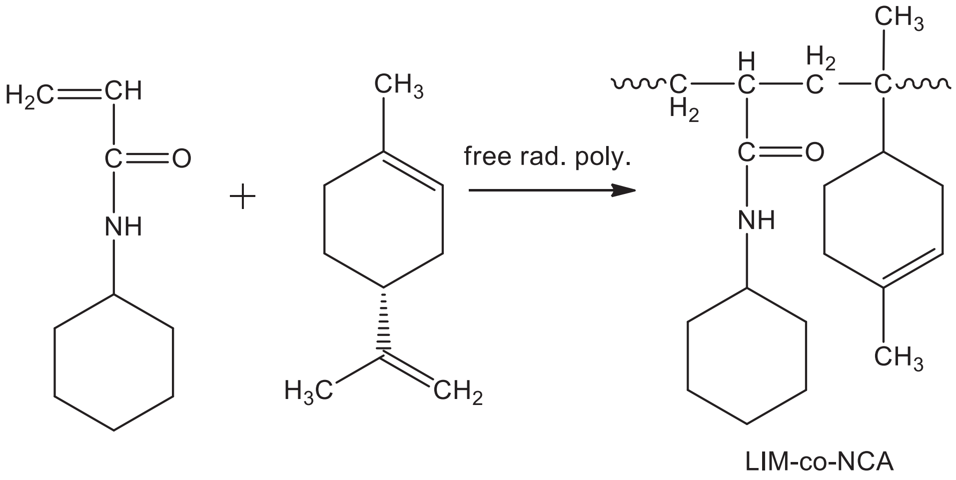

FIGURE 1 | Synthesis of copolymer LIM-*co*-NCA.

monomers, NCA (153 mg, 1 mmol) and D-limonene (136 mg, 1 mmol), with the radical initiator benzoyl peroxide in 10 mL 1,4-dioxane solution were added to the polymerization flask. The reaction solution was mixed under argon atmosphere at 70°C for 36 h. The mixture solution was cooled. The resulting copolymer was crystallized to remove impurities with ethyl alcohol three times [13].

Synthesis of limonene with NCA (LIM-*co*-NCA) is shown in Figure 1. The chemical structure of the copolymer was characterized by spectroscopic methods (FT-IR, ^{1}H-NMR). The molecular weight of LIM-*co*-NCA was detected by GPC.

FT-IR (ATR, cm^{-1}): 3294 (N—H), 1643 (C═O), 1534 (O═C—NH), 2930 (—CH$_2$), 2852 (—CH$_3$).

^{1}H-(400 MHz, CDCl3): δ (ppm): 8.4 (s: —NH), 7.5–7.3 (m: ArH), 6.8–6.6 (m: ArH), 4.4–4.2 (m: endocyclic-exocyclic —CH Cyclohexene), 3.7 (s: —OCH3), 2.2–1.8 (m: —CH2, Cyclohexene), 1.5 (m: polymer chain —CH2), 1.3 (m: —CH, Cyclohexene).

2.3 | Cell Proliferation Assay

Human cervix adenocarcinoma (HeLa) cells were cultured in RPMI 1640 supplemented with 10% FBS and 1% penicillin–streptomycin (Gibco), and they were maintained at 37°C in a humidified 5% CO$_2$ atmosphere. Cell Proliferation Kit (XTT) (Biological Ind.) was used according to the manufacturer's protocol. The absorbance is read at 450 nm by a spectrophotometer (BIOTEK). All analyses were performed in triplicates as specified.

2.4 | Computational Analyses

2.4.1 | DFT Calculations

The ligand optimization processes were carried out using the Gaussian09 software [14]. The geometric optimization of the compounds was performed using the DFT method with the B3LYP exchange–correlation hybrid functional and the 6–31G(d) [15, 16] basis set (Figure 2). All optimizations were performed until the Gaussian09 default convergence criteria were satisfied. Specifically, the thresholds applied were: maximum force ≤ 0.00045 Hartree/Bohr, RMS force ≤ 0.00030 Hartree/Bohr, maximum displacement ≤ 0.0018 Å, RMS displacement ≤ 0.0012 Å, and total energy change $< 1.0 \times 10^{-6}$ Hartree.

2.4.2 | Molecular Docking

Molecular docking studies were carried out to investigate the binding affinities of Comp1, Comp2, and Comp3 with the 3FAA and 6GUB receptors. Docking calculations were performed using AutoDock Vina [17] and ligands were docked into the prepared receptor structures after geometry optimization at the DFT level. For each ligand–receptor pair, the best binding pose was selected based on the lowest binding energy score and favorable orientation within the active site. The resulting complexes were subsequently used as the initial structures for MD simulations.

2.4.3 | MD Simulations

To evaluate the stability and dynamic behavior of the ligand–receptor complexes, mMD simulations were performed using GROMACS [18]. The AMBER19SB force field was employed to parameterize the proteins, while ligand parameters were generated using the GAFF force field. Each system was solvated in a TIP3P water box with periodic boundary conditions and neutralized by adding counterions. Energy minimization was carried out to remove steric clashes, followed by equilibration steps in the NVT and NPT ensembles.

Production MD runs were conducted for 100 ns with a time step of 2 fs to better capture long–term conformational fluctuations and ensure statistically robust sampling. The leap–frog integrator was used, and system temperature (300 K) was controlled using the V–rescale thermostat, while pressure (1 bar) was maintained using the Parrinello–Rahman barostat. Long–range electrostatic interactions were treated with the Particle Mesh Ewald (PME) method, and a 1.4 nm cutoff was

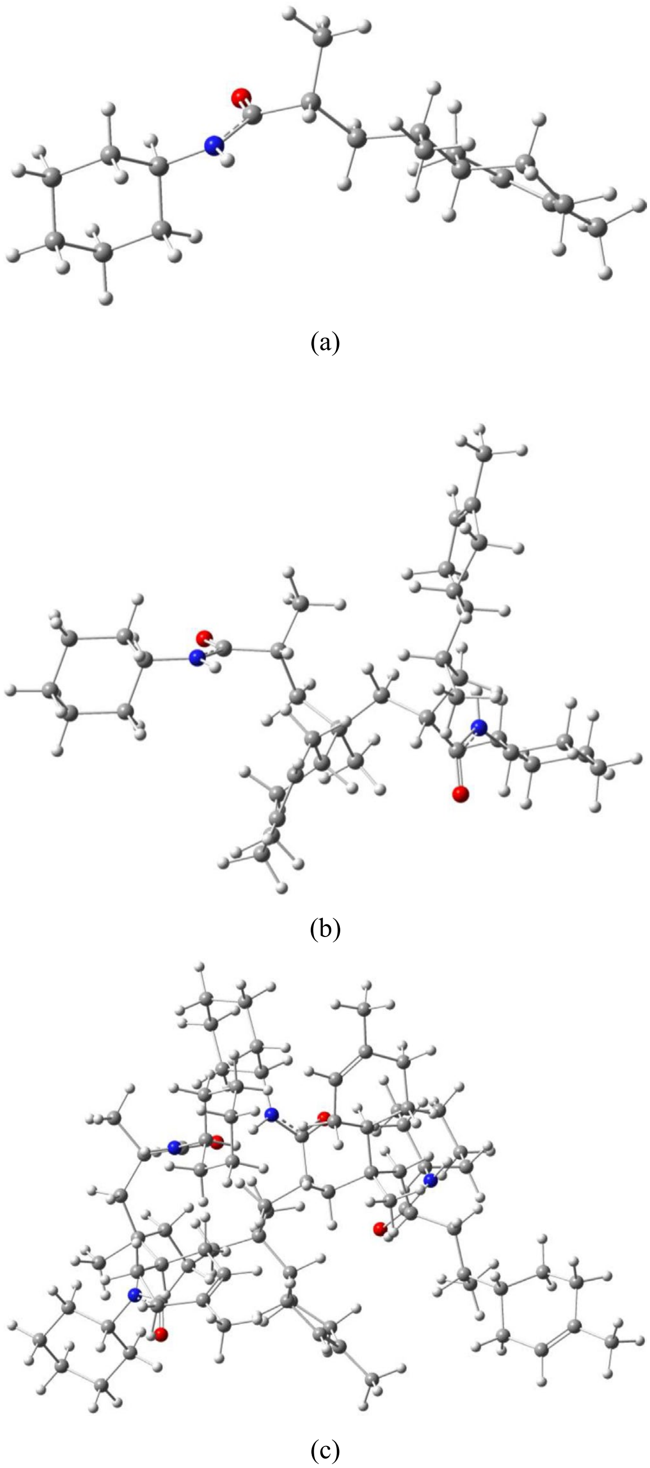

(a)

(b)

(c)

FIGURE 2 | Optimized structures of (a) comp1, (b) comp2, and (c) comp3 compounds.

applied for short–range electrostatics and van der Waals interactions. Trajectories were recorded every 10 ps for subsequent analyses.

2.4.4 | Total Binding Energy Calculations

Total binding energies were calculated using the Molecular Mechanics Poisson–Boltzmann Surface Area (MMPBSA) method [19]. The calculations were performed with the gmx_MMPBSA v1.5.0 tool, with the initial frame number set to 1, and all frames were analyzed. The simulations were conducted at a temperature of 300 K, incorporating the Interaction Entropy (IE) contribution to account for entropic effects. Additionally, C2 entropy was included in the computations. The Poisson–Boltzmann model was configured with the pb_radii option set to 3, while the Generalized–Born (GB) solvation model was applied with the igb = 5 option, and the salt concentration was set to 0.154 M.

In the binding energy calculations, electrostatic interactions, van der Waals forces, and both polar and nonpolar solvation energies were considered. Alongside the Poisson–Boltzmann and Generalized–Born models, the Interaction Entropy (IE) method was employed to incorporate entropic contributions into the free energy calculations. These calculations enhance the accuracy of binding energy estimations.

3 | Results and Discussion

3.1 | Spectroscopic Characterization of LIM-*co*-NCA

The synthesis of copolymer LIM-*co*-NCA was carried out by free radical polymerization of NCA and D-limonene in the presence of benzoylperoxide as an initiator. The reaction scheme for the synthesis of copolymer LIM-*co*-NCA is given in Figure 1. The chemical structure of the LIM-*co*-NCA was confirmed by FT-IR and ^{1}H-NMR. The recommended structure is in full agreement with all spectroscopic data. The FT-IR spectrum of the copolymer is shown in Figure 3. The ^{1}H-NMR spectrum of LIM-*co*-NCA is shown in Figure 4.

The FT-IR spectrum of LIM-*co*-NCA displayed –NH, C═O, and O═C-NH typical stretching bands at 3294, 1643, and 1534 cm^{-1}, respectively.

The structure of the copolymer can be identified by comparing the ^{1}H-NMR spectrum of the monomer NCA and D-limonene copolymer. The ^{1}H-NMR spectrum of the monomer NCA revealed two multiples in the range of 4.5–4.6 ppm olefinic protons (1H, CH and 2H, CH$_2$). As seen in the ^{1}H-NMR spectrum of LIM-*co*-NCA (Figure 4), olefinic protons in the range of 4.5–4.6 ppm are not observed.

3.2 | Thermal and chromatographic Characterization of LIM-*co*-NCA

The thermal properties of LIM-*co*-NCA determined by thermal gravimetric analysis/differential thermal gravimetry (TGA/DTG). The temperature at 50% weight loss is taken as a measure of thermal stability. It has been observed that degradation from the thermogram occurs at one level. Important values for the copolymer of Limonene with NCA are: Decomposition temperature at 30% is 356°C, decomposition temperature at 50% is 395°C, weight loss at 300°C is 18%, weight loss at 400°C is 55%, residue at 450°C and 500°C is 6% and 0%, respectively. Also, the maximum decomposition temperature is 415°C, and the initial

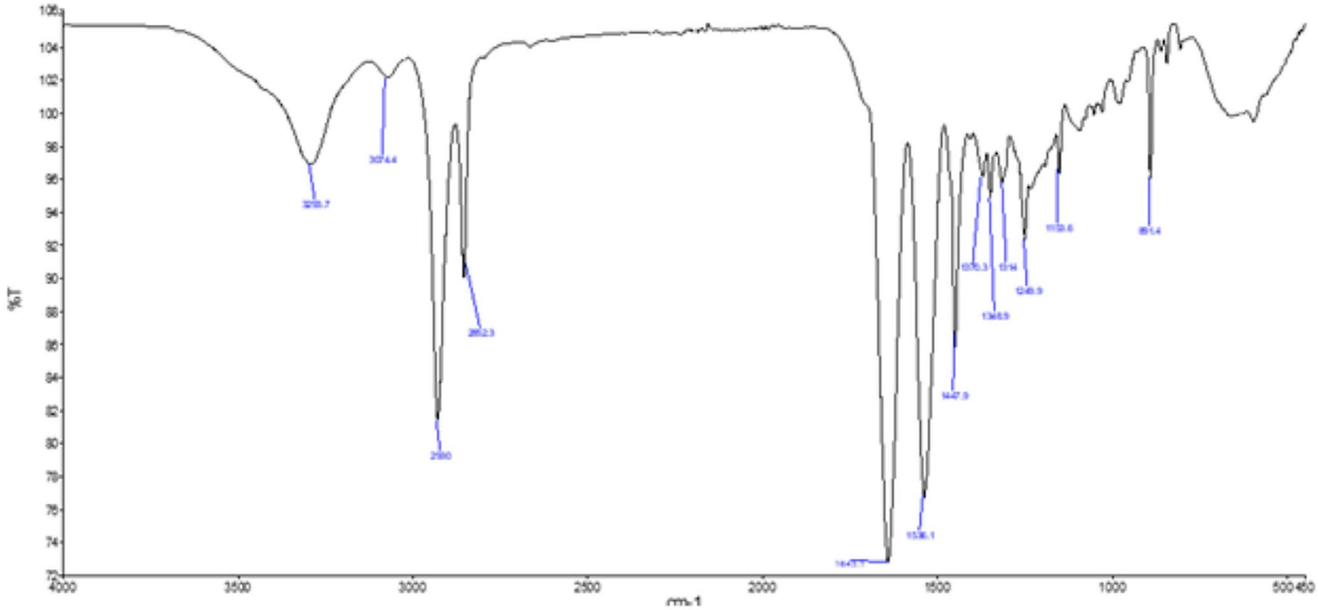

FIGURE 3 | FT-IR spectra of LIM-*co*-NCA.

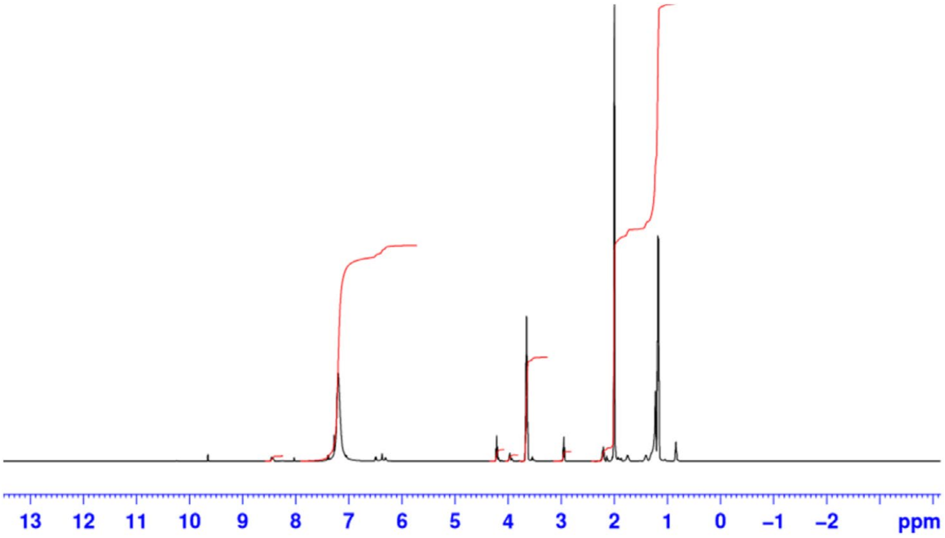

FIGURE 4 | The ^{1}H-NMR spectrum of LIM-*co*-NCA.

decomposition temperature is ~160°C. The TGA/DTG curves of the copolymer are given in Figure 5.

Molecular weight and molecular weight distribution of copolymer was detected by GPC. The highest molecular weight of the LIM-*co*-NCA (weight-average molecular weight (M_w) = 3499, number-average molecular weight (M_n) = 2155) was determined and heterogeneity index (HI) of copolymer (M_w/M_n) = 1.62 was detected by GPC based on polystyrene standards. The GPC plots of LIM-*co*-NCA are shown in Figure 6.

3.3 | Antiproliferative Activity on *He-La* Cell Line

As shown in Figure 7, the proliferation of *He-La* cells significantly declined after treatment with LIM-*co*-NCA for 48 h. In this study, cancer cell lines were stimulated with LIM-*co*-NCA in different doses (concentration range 0–500 μg/mL) in vitro experiments. It was found in the XTT assay that the LIM-*co*-NCA significantly inhibited the proliferation of the He-La cells (IC50 values 148.15 μg/mL).

3.4 | Molecular Docking Analysis

The crystal structures of the target proteins (3FAA and 6GUB) were retrieved from the Protein Data Bank (PDB). Water molecules were removed, polar hydrogens were added, and Gasteiger charges were assigned.

The docking grid box was defined to fully encompass the active site residues of each receptor. For the 3FAA receptor, the

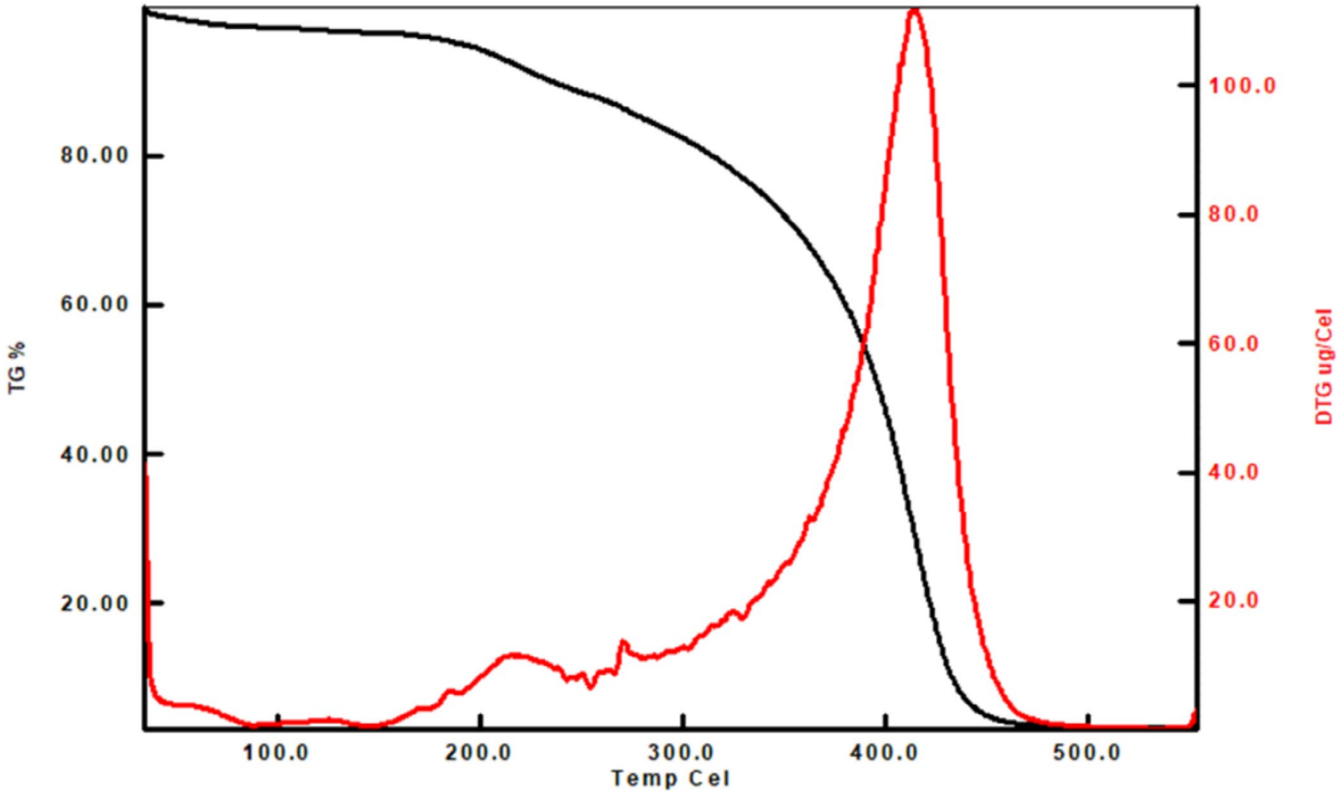

FIGURE 5 | TGA/DTG curves of LIM-*co*-NCA.

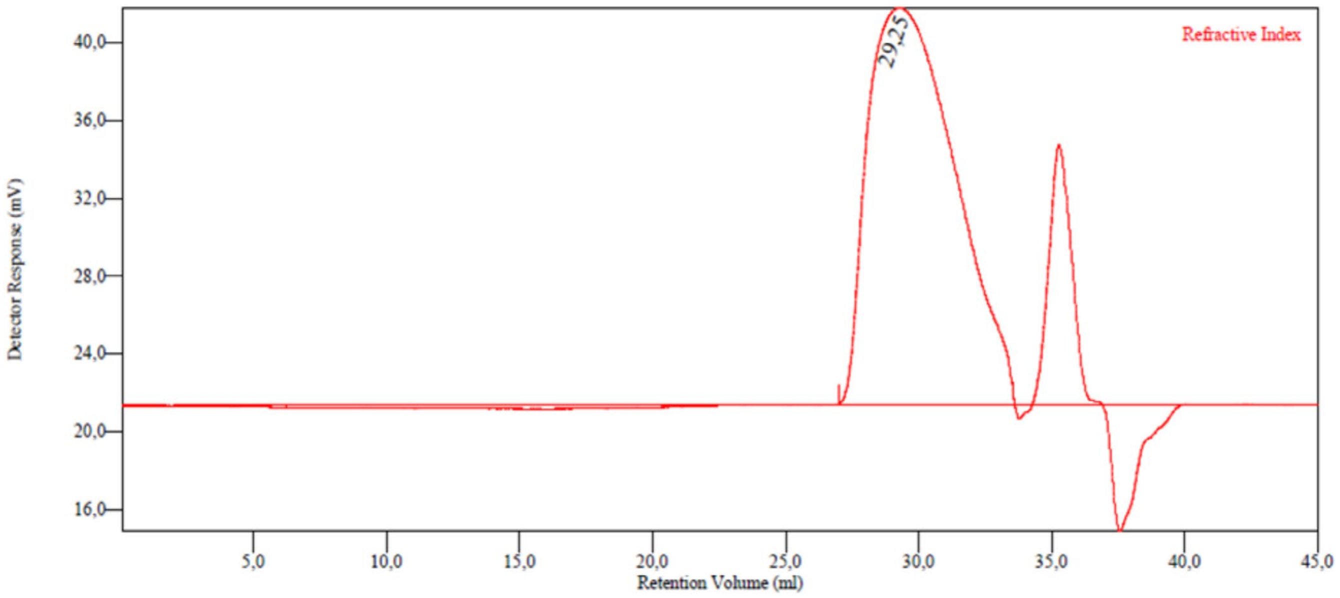

FIGURE 6 | GPC curve of the LIM-*co*-NCA.

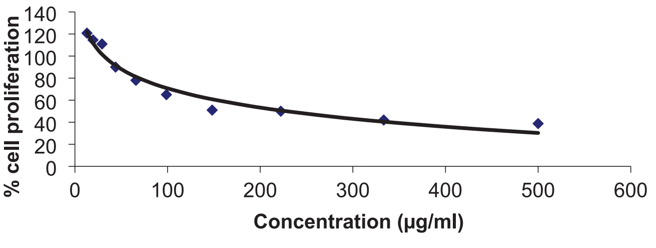

FIGURE 7 | LIM-*co*-NCA inhibits proliferation of HeLa cells.

grid box was centered at ($x=48.24$, $y=42.96$, $z=37.12$ Å), while for the 6GUB receptor, the grid box was centered at ($x=25.59$, $y=37.71$, $z=36.39$ Å). The grid box dimensions were chosen to adequately cover the binding pocket in each case, ensuring that all potential binding modes of the ligands were sampled.

Docking results were ranked according to binding affinity (kcal/mol), and the top-ranked poses were selected for subsequent MD simulations. Hydrogen bonding interactions, hydrophobic contacts, and π–π stacking interactions were analyzed using Discovery Studio Visualizer. Key residues involved in ligand binding were identified, and interatomic distances were measured. This docking analysis served as an initial validation of binding stability, which was further confirmed through MD simulations.

The docking results of Comp1, Comp2, and Comp3 with the 3FAA receptor are visualized in Figure 2 and presented in Tables 1–3, providing a detailed view of their binding modes and interaction profiles. For 3FAA–Comp1, the binding affinity was calculated as −9.9 kcal/mol, representing the strongest interaction among the three ligands. The ligand forms short–range hydrogen bonds with SER110 and GLU75, indicating that its binding pose is stabilized through pronounced polar contributions. These strong and directional contacts suggest that Comp1 anchors specifically and energetically favorably within the receptor pocket.

In the case of 3FAA–Comp2, the binding score was −9.2 kcal/mol, slightly weaker than that of Comp1. Nevertheless, the presence of a strong hydrogen bond with LEU84 and an additional carbon–hydrogen interaction with GLY91 demonstrates that the ligand is properly oriented within the active site. Although the overall binding energy is lower compared to Comp1, the regular and stable nature of these interactions supports the ligand's retention in the pocket.

For 3FAA–Comp3, the binding affinity was −9.4 kcal/mol. Despite this relatively favorable energy, the binding mode is not characterized by strong hydrogen bonds but rather by hydrophobic alkyl–alkyl contacts involving ALA60 and LYS62. Due to the bulky and branched nature of the molecule, several amide groups are oriented toward the solvent rather than into the binding cavity, thereby limiting hydrogen bond contributions. Nevertheless, extensive hydrophobic surface contacts sustain a binding score that remains comparatively strong.

In comparative terms, Comp1 achieves the most favorable interaction through polar anchoring, while Comp3 relies predominantly on hydrophobic contacts as an alternative stabilization strategy. Comp2, although associated with the weakest docking score, displays a balanced interaction profile with stable hydrogen–bonding and supportive hydrophobic contacts. These findings, supported by both Figure 8 and Tables 1–3, emphasize distinct binding strategies: Comp1 excels in polar stabilization, Comp3 in hydrophobic complementarity, and Comp2 in maintaining an intermediate, well–balanced binding mode within the 3FAA receptor pocket.

The docking results of Comp1, Comp2, and Comp3 with the 6GUB receptor are visualized in Figure 3 and presented in Tables 4–6, highlighting distinct binding preferences among the ligands. For 6GUB–Comp1, the binding affinity was calculated as −7.5 kcal/mol, the weakest score among the three. The interaction profile is dominated by hydrophobic alkyl–alkyl contacts with ILE10 and ALA31, while no hydrogen bonds were detected. This binding mode suggests that Comp1 relies primarily on van der Waals complementarity to occupy the binding cavity, yet the absence of directional hydrogen bonds may limit its stability and specificity.

In the case of 6GUB–Comp2, the binding score improved to −8.8 kcal/mol. The ligand establishes a conventional hydrogen bond with LYS142 (2.99 Å) and a carbon–hydrogen interaction with ASP145 (2.68 Å). These polar contacts, in combination with the hydrophobic fit, indicate a stronger and more specific interaction compared to Comp1. The dual contribution of electrostatic and hydrophobic forces enhances the overall binding affinity, making Comp2 a more promising candidate within this receptor pocket.

For 6GUB–Comp3, the binding affinity reached −9.3 kcal/mol, the strongest value among the three ligands in this receptor. The interaction network involves a carbon–hydrogen bond with ASN132 (2.7 Å) alongside hydrophobic contact with ILE10 (5.18 Å). This dual interaction pattern suggests that Comp3 benefits from both polar and nonpolar contributions, which together stabilize its binding conformation. The relatively balanced profile explains its superior docking score compared to Comp1 and Comp2.

When compared, Comp1 exhibits the weakest interaction, relying solely on hydrophobic embedding without hydrogen–bond support. Comp2 demonstrates a marked improvement by introducing specific polar contacts, while Comp3 achieves the strongest binding affinity through a balanced combination of hydrogen bonding and hydrophobic interactions. These results, as summarized in Tables 4–6 and depicted in Figure 9, indicate that in the 6GUB receptor, Comp3 emerges as the most favorable ligand, followed by Comp2, whereas Comp1 shows the least effective binding.

The comparative analysis of docking results between the 3FAA and 6GUB receptor systems reveals distinct ligand preferences and interaction strategies. In the 3FAA receptor, Comp1 achieved the strongest binding affinity (−9.9 kcal/mol), primarily driven by two short hydrogen bonds with SER110 and GLU75, underscoring the importance of polar anchoring in stabilizing the complex. Comp3 (−9.4 kcal/mol) displayed comparable affinity but relied predominantly on hydrophobic contacts with ALA60 and LYS62, while Comp2 (−9.2 kcal/mol) adopted an intermediate mode characterized by fewer but stable hydrogen–bond interactions with LEU84 and GLY91. These results suggest that in 3FAA, Comp1 is favored due to strong electrostatic complementarity, whereas Comp3 benefits from broad hydrophobic complementarity. In the 6GUB receptor, the order of binding affinity was reversed. Comp3 exhibited the strongest score (−9.3 kcal/mol) by combining a hydrogen bond with ASN132 and hydrophobic contacts with ILE10, reflecting a balanced polar–nonpolar stabilization. Comp2 (−8.8 kcal/mol) followed closely, supported by directional polar contacts with LYS142 and ASP145. In contrast, Comp1 displayed the weakest affinity (−7.5 kcal/mol), relying solely on hydrophobic interactions with ILE10 and ALA31, which provided insufficient stabilization compared to the other two ligands. Taken together, the docking analysis highlights receptor–specific preferences: in 3FAA, polar anchoring interactions gave Comp1 the highest advantage, whereas in 6GUB, the best performance shifted to Comp3, whose balanced polar and hydrophobic interactions optimized its binding. These complementary results emphasize that ligand efficiency is strongly dependent on the chemical

TABLE 1 | Interaction profile of the 3FAA–Comp1 complex.

Name	Distance	Interaction	Types	Donor group	Donor atom	Acceptor group	Acceptor atom	DHA (°)
SER110:HG—UNK:O	2.10	Hydrogen Bond	Conventional Hydrogen Bond	SER110:HG	H-Donor	UNK:O	H-Acceptor	150
UNK:H4-GLU75:OE2	2.63	Hydrogen Bond	Conventional Hydrogen Bond	UNK:H4	H-Donor	GLU75:OE2	H-Acceptor	155
SER110:HB3- UNK:O	2.76	Hydrogen Bond	Carbon Hydrogen Bond	SER110:HB3	H-Donor	UNK:O	H-Acceptor	113
VAL49-UNK	5.40	Hydrophobic	Alkyl	VAL49	Alkyl	UNK	Alkyl	—
ALA60-UNK	5.12	Hydrophobic	Alkyl	ALA60	Alkyl	UNK	Alkyl	—
LYS62-UNK	4.41	Hydrophobic	Alkyl	LYS62	Alkyl	UNK	Alkyl	—
ALA76-UNK	5.06	Hydrophobic	Alkyl	ALA76	Alkyl	UNK	Alkyl	—
ALA76-UNK:C18	4.41	Hydrophobic	Alkyl	ALA76	Alkyl	UNK:C18	Alkyl	—
ALA95-UNK:C18	3.83	Hydrophobic	Alkyl	ALA95	Alkyl	UNK:C18	Alkyl	—
LEU108-UNK	4.98	Hydrophobic	Alkyl	LEU108	Alkyl	UNK	Alkyl	—
UNK:C18-LEU108	4.06	Hydrophobic	Alkyl	UNK:C18	Alkyl	LEU108	Alkyl	—
TYR79-UNK:C12	4.04	Hydrophobic	Pi-Alkyl	TYR79	Pi-Orbitals	UNK:C12	Alkyl	—
PHE92-UNK	4.25	Hydrophobic	Pi-Alkyl	PHE92	Pi-Orbitals	UNK	Alkyl	—

Note: The table summarizes hydrogen bonds and hydrophobic interactions between protein residues and the ligand, indicating donor/acceptor groups, atoms, bond distances, and types of interactions.

TABLE 2 | Interaction profile of the 3FAA–Comp2 complex.

Name	Distance	Interaction	Types	Donor group	Donor atom	Acceptor group	Acceptor atom	DHA (°)
UNK:H37-LEU84:O	2.07	Hydrogen Bond	Conventional Hydrogen Bond	UNK:H37	H-Donor	LEU84:O	H-Acceptor	149
GLY91:HA2-UNK:O	2.66	Hydrogen Bond	Carbon Hydrogen Bond	GLY91:HA2	H-Donor	UNK:O	H-Acceptor	136
ILE11-UNK	4.64	Hydrophobic	Alkyl	ILE11	Alkyl	UNK	Alkyl	—
ARG85-UNK	4.29	Hydrophobic	Alkyl	ARG85	Alkyl	UNK	Alkyl	—
ARG85-UNK	4.40	Hydrophobic	Alkyl	ARG85	Alkyl	UNK	Alkyl	—
ALA180-UNK:C37	4.30	Hydrophobic	Alkyl	ALA180	Alkyl	UNK:C37	Alkyl	—
UNK:C-MET14	4.74	Hydrophobic	Alkyl	UNK:C	Alkyl	MET14	Alkyl	—
UNK:C18-MET83	4.85	Hydrophobic	Alkyl	UNK:C18	Alkyl	MET83	Alkyl	—
UNK:C18-ARG85	4.16	Hydrophobic	Alkyl	UNK:C18	Alkyl	ARG85	Alkyl	—
UNK:C37-LEU90	4.47	Hydrophobic	Alkyl	UNK:C37	Alkyl	LEU90	Alkyl	—
TYR79-UNK	3.79	Hydrophobic	Pi-Alkyl	TYR79	Pi-Orbitals	UNK	Alkyl	—

Note: The table summarizes hydrogen bonds and hydrophobic interactions between protein residues and the ligand, indicating donor/acceptor groups, atoms, bond distances, and types of interactions.

environment of the binding site, and that different receptor topologies favor distinct binding strategies.

3.5 | MD Simulations and Comparative Stability Analysis

MD simulations are computational techniques that allow for the detailed investigation of atomic and molecular movements and interactions over time [20]. These simulations provide valuable insights into the dynamic behavior and evolution of molecular systems. Traditional experimental methods often have limitations in terms of the conditions they can explore and the level of detail they can provide. In contrast, MD simulations enable the examination of molecular behavior under various realistic conditions, including changes in temperature, pressure, and solubility, thereby offering a more comprehensive perspective [21].

These simulations allow for the real–time observation and analysis of interactions among multiple molecular components. For instance, they are particularly useful for studying receptor–ligand interactions, biomolecular conformational changes, and reaction mechanisms [20, 21]. Experimental approaches may sometimes fall short in capturing such intricate details, whereas MD simulations offer a more complete understanding of the long–term dynamic properties of molecular systems [22]. As a result, they contribute significantly to our understanding of how molecular structures respond to different environmental conditions.

In this study, the Amber software package was used to generate the initial structural model of the protein–ligand complex, and the necessary input files for the simulation were prepared. The AMBER ff14SB force field and GAFF parameterization were applied in this process. To ensure proper solvation, the protein–ligand complex was immersed in a TIP3P water box with an 8 Å buffer, and the system's net charge was balanced using Cl^- and Na^+ ions. The final system configuration was saved as prmtop and inpcrd files, which were subsequently used as input for GROMACS simulations. Additionally, utilizing the generated gro and topology files, a Cl^- ion was introduced to neutralize each system (Figure 10).

The constructed system underwent a series of simulations, including NVT, NPT, and MD phases. During the NVT equilibration, the system was stabilized at 300 K. The leap–frog algorithm ('md' integrator) was employed for a total of 50,000 steps. To maintain structural integrity while reaching thermal equilibrium, positional restraints were applied to the protein and ligand. Temperature regulation was achieved using the V–rescale thermostat, which independently controlled the temperature of the protein, ligand, water, and ions. Initial velocities were assigned randomly based on a Maxwell–Boltzmann distribution, with the system starting at 300 K.

In the NPT equilibration phase, the system's pressure and density were stabilized. Following the completion of the NVT stage, the leap–frog integration continued for another 50,000 steps. The V–rescale thermostat ensured temperature control, while the Parrinello–Rahman barostat regulated the pressure. The system was equilibrated under isotropic pressure conditions,

TABLE 3 | Interaction profile of the 3FAA–Comp3 complex.

Name	Distance	Interaction	Types	Donor group	Donor atom	Acceptor group	Acceptor atom	DHA (°)
ALA60-UNK	3.74	Hydrophobic	Alkyl	ALA60	Alkyl	UNK	Alkyl	—
LYS6-UNK	5.31	Hydrophobic	Alkyl	LYS62	Alkyl	UNK	Alkyl	—
LEU108-UNK	4.61	Hydrophobic	Alkyl	LEU108	Alkyl	UNK	Alkyl	—
LYS167-UNK	5.45	Hydrophobic	Alkyl	LYS167	Alkyl	UNK	Alkyl	—
LEU170-UNK	4.93	Hydrophobic	Alkyl	LEU170	Alkyl	UNK	Alkyl	—
ALA180-UNK	4.70	Hydrophobic	Alkyl	ALA180	Alkyl	UNK	Alkyl	—
LEU184-UNK	5.48	Hydrophobic	Alkyl	LEU184	Alkyl	UNK	Alkyl	—
UNK:C21-LYS167	3.64	Hydrophobic	Alkyl	UNK:C21	Alkyl	LYS167	Alkyl	—
UNK:C42-LYS167	4.58	Hydrophobic	Alkyl	UNK:C42	Alkyl	LYS167	Alkyl	—
UNK:C63-LEU184	4.38	Hydrophobic	Alkyl	UNK:C63	Alkyl	LEU184	Alkyl	—
UNK:C84-VAL203	4.66	Hydrophobic	Alkyl	UNK:C84	Alkyl	VAL203	Alkyl	—
PHE64-UNK	5.47	Hydrophobic	Pi-Alkyl	PHE64	Pi-Orbitals	UNK	Alkyl	—
PHE119-UNK:C21	5.37	Hydrophobic	Pi-Alkyl	PHE119	Pi-Orbitals	UNK:C21	Alkyl	—

Note: The table summarizes hydrogen bonds and hydrophobic interactions between protein residues and the ligand, indicating donor/acceptor groups, atoms, bond distances, and types of interactions.

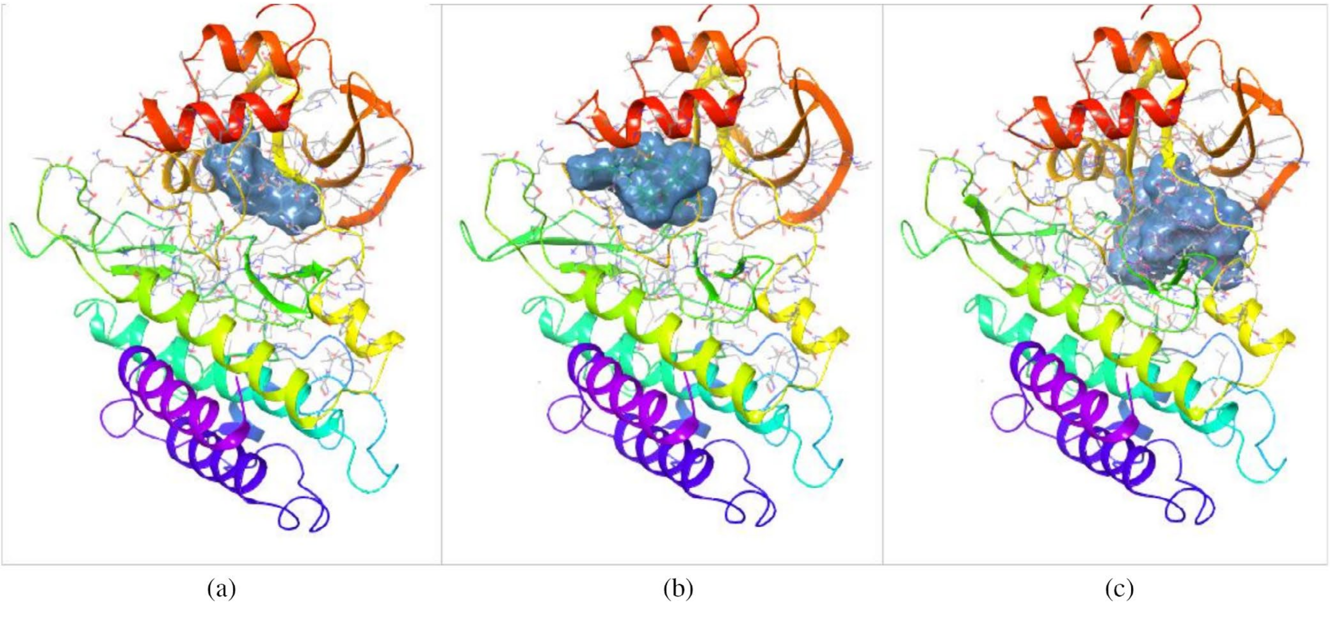
(a) (b) (c)

FIGURE 8 | Binding pocket representations of the 3FAA protein in complex with different compounds. (a) 3FAA–comp1, (b) 3FAA–comp2, and (c) 3FAA–comp3.

maintaining a reference pressure of 1 bar. Throughout this process, the simulation box volume was dynamically adjusted, leading to density stabilization. The velocities established in the NVT phase were retained without reassignment.

For the production phase, MD simulations were conducted over 100 ns. The system was simulated for 50,000,000 steps, with coordinate and energy data recorded every 10 ps. The V-rescale thermostat and Parrinello–Rahman barostat were utilized to

TABLE 4 | Interaction profile of the 6GUB–Comp1 complex.

Name	Distance	Interaction	Types	Donor group	Donor atom	Acceptor group	Acceptor atom	DHA (°)
ILE10-UNK	4.35	Hydrophobic	Alkyl	ILE10	Alkyl	UNK	Alkyl	—
ALA31-UNK	4.96	Hydrophobic	Alkyl	ALA31	Alkyl	UNK	Alkyl	—
LYS33-UNK	4.35	Hydrophobic	Alkyl	LYS33	Alkyl	UNK	Alkyl	—
LEU134-UNK	4.40	Hydrophobic	Alkyl	LEU134	Alkyl	UNK	Alkyl	—
ALA144-UNK	5.07	Hydrophobic	Alkyl	ALA144	Alkyl	UNK	Alkyl	—
ALA144-UNK:C18	4.15	Hydrophobic	Alkyl	ALA144	Alkyl	UNK:C18	Alkyl	—
UNK:C12-VAL18	4.30	Hydrophobic	Alkyl	UNK:C12	Alkyl	VAL18	Alkyl	—
UNK:C12-LYS33	4.67	Hydrophobic	Alkyl	UNK:C12	Alkyl	LYS33	Alkyl	—
UNK:C18-VAL64	3.94	Hydrophobic	Alkyl	UNK:C18	Alkyl	VAL64	Alkyl	—
PHE80-UNK:C18	3.51	Hydrophobic	Pi-Alkyl	PHE80	Pi-Orbitals	UNK:C18	Alkyl	—

Note: The table summarizes hydrogen bonds and hydrophobic interactions between protein residues and the ligand, indicating donor/acceptor groups, atoms, bond distances, and types of interactions.

TABLE 5 | Interaction profile of the 6GUB–Comp2 complex.

Name	Distance	Interaction	Types	Donor group	Donor atom	Acceptor group	Acceptor atom	DHA (°)
LYS142:HZ3-UNK:O1	2.99	Hydrogen Bond	Conventional Hydrogen Bond	LYS142:HZ3	H-Donor	UNK:O1	H-Acceptor	135
UNK:H5-ASP145:OD2	2.68	Hydrogen Bond	Carbon Hydrogen Bond	UNK:H5	H-Donor	ASP145:OD2	H-Acceptor	139
ILE10-UNK	5.36	Hydrophobic	Alkyl	ILE10	Alkyl	UNK	Alkyl	—
VAL18-UNK	5.47	Hydrophobic	Alkyl	VAL18	Alkyl	UNK	Alkyl	—
VAL18-UNK	5.44	Hydrophobic	Alkyl	VAL18	Alkyl	UNK	Alkyl	—
VAL64-UNK	4.97	Hydrophobic	Alkyl	VAL64	Alkyl	UNK	Alkyl	—
LYS65-UNK	5.19	Hydrophobic	Alkyl	LYS65	Alkyl	UNK	Alkyl	—
LEU134-UNK	5.25	Hydrophobic	Alkyl	LEU134	Alkyl	UNK	Alkyl	—
LYS142-UNK	5.03	Hydrophobic	Alkyl	LYS142	Alkyl	UNK	Alkyl	—
UNK:C30-LEU134	4.65	Hydrophobic	Alkyl	UNK:C30	Alkyl	LEU134	Alkyl	—
UNK:C37-ILE10	3.97	Hydrophobic	Alkyl	UNK:C37	Alkyl	ILE10	Alkyl	—

Note: The table summarizes hydrogen bonds and hydrophobic interactions between protein residues and the ligand, indicating donor/acceptor groups, atoms, bond distances, and types of interactions.

maintain a consistent temperature of 300 K and a pressure of 1 bar. Periodic boundary conditions (PBC) were applied throughout the simulation. The Verlet cutoff scheme was implemented for short-range interactions, with van der Waals and electrostatic interactions confined to a 1.4 nm cutoff distance. Meanwhile, long-range electrostatic interactions were computed using the Particle Mesh Ewald (PME) method.

This simulation workflow facilitated a systematic transition from energy minimization to the production phase. The simulation results, including parameters such as temperature, pressure, total energy, and root–mean–square deviation (RMSD), were thoroughly analyzed to assess the system's dynamic behavior. A higher potential energy implies lower overall thermodynamic stability of the system [23].

TABLE 6 | Interaction profile of the 6GUB–Comp3 complex.

Name	Distance	Interaction	Types	Donor group	Donor atom	Acceptor group	Acceptor atom	DHA (°)
ASN132:HA-UNK:O46	2.70	Hydrogen Bond	Carbon Hydrogen Bond	ASN132:HA	H-Donor	UNK:O46	H-Acceptor	135
ILE10-UNK	5.18	Hydrophobic	Alkyl	ILE10	Alkyl	UNK	Alkyl	—
VAL18-UNK	5.25	Hydrophobic	Alkyl	VAL18	Alkyl	UNK	Alkyl	—
VAL18-UNK	5.21	Hydrophobic	Alkyl	VAL18	Alkyl	UNK	Alkyl	—
ALA31-UNK:C42	4.27	Hydrophobic	Alkyl	ALA31	Alkyl	UNK:C42	Alkyl	—
ALA31-UNK	4.86	Hydrophobic	Alkyl	ALA31	Alkyl	UNK	Alkyl	—
ALA31-UNK:C84	3.41	Hydrophobic	Alkyl	ALA31	Alkyl	UNK:C84	Alkyl	—
LYS33-UNK	4.36	Hydrophobic	Alkyl	LYS33	Alkyl	UNK	Alkyl	—
ILE35-UNK	4.94	Hydrophobic	Alkyl	ILE35	Alkyl	UNK	Alkyl	—
ALA48-UNK	4.83	Hydrophobic	Alkyl	ALA48	Alkyl	UNK	Alkyl	—
ALA48-UNK:C21	4.00	Hydrophobic	Alkyl	ALA48	Alkyl	UNK:C21	Alkyl	—
VAL64-UNK	4.67	Hydrophobic	Alkyl	VAL64	Alkyl	UNK	Alkyl	—
LEU134-UNK	4.26	Hydrophobic	Alkyl	LEU134	Alkyl	UNK	Alkyl	—
ALA144-UNK	4.01	Hydrophobic	Alkyl	ALA144	Alkyl	UNK	Alkyl	—
LEU148-UNK	4.81	Hydrophobic	Alkyl	LEU148	Alkyl	UNK	Alkyl	—
UNK:C21-ILE35	3.51	Hydrophobic	Alkyl	UNK:C21	Alkyl	ILE35	Alkyl	—
UNK:C21-PRO45	3.89	Hydrophobic	Alkyl	UNK:C21	Alkyl	PRO45	Alkyl	—
UNK:C42-VAL18	4.72	Hydrophobic	Alkyl	UNK:C42	Alkyl	VAL18	Alkyl	—
UNK:C42-LYS33	4.24	Hydrophobic	Alkyl	UNK:C42	Alkyl	LYS33	Alkyl	—
UNK:C63-ILE10	5.49	Hydrophobic	Alkyl	UNK:C63	Alkyl	ILE10	Alkyl	—
UNK:C84-LEU134	5.08	Hydrophobic	Alkyl	UNK:C84	Alkyl	LEU134	Alkyl	—
TYR15-UNK:C21	4.66	Hydrophobic	Pi-Alkyl	TYR15	Pi-Orbitals	UNK:C21	Alkyl	—
PHE80-UNK:C42	4.59	Hydrophobic	Pi-Alkyl	PHE80	Pi-Orbitals	UNK:C42	Alkyl	—

Note: The table summarizes hydrogen bonds and hydrophobic interactions between protein residues and the ligand, indicating donor/acceptor groups, atoms, bond distances, and types of interactions.

The potential energy variations of the systems formed by Comp1, Comp2, and Comp3 ligands with 3FAA and 6GUB receptors were analyzed, revealing that each system reached different energy levels over time and approached equilibrium at different rates. In all systems, a rapid decrease in energy was observed at the beginning of the simulation, followed by stabilization into

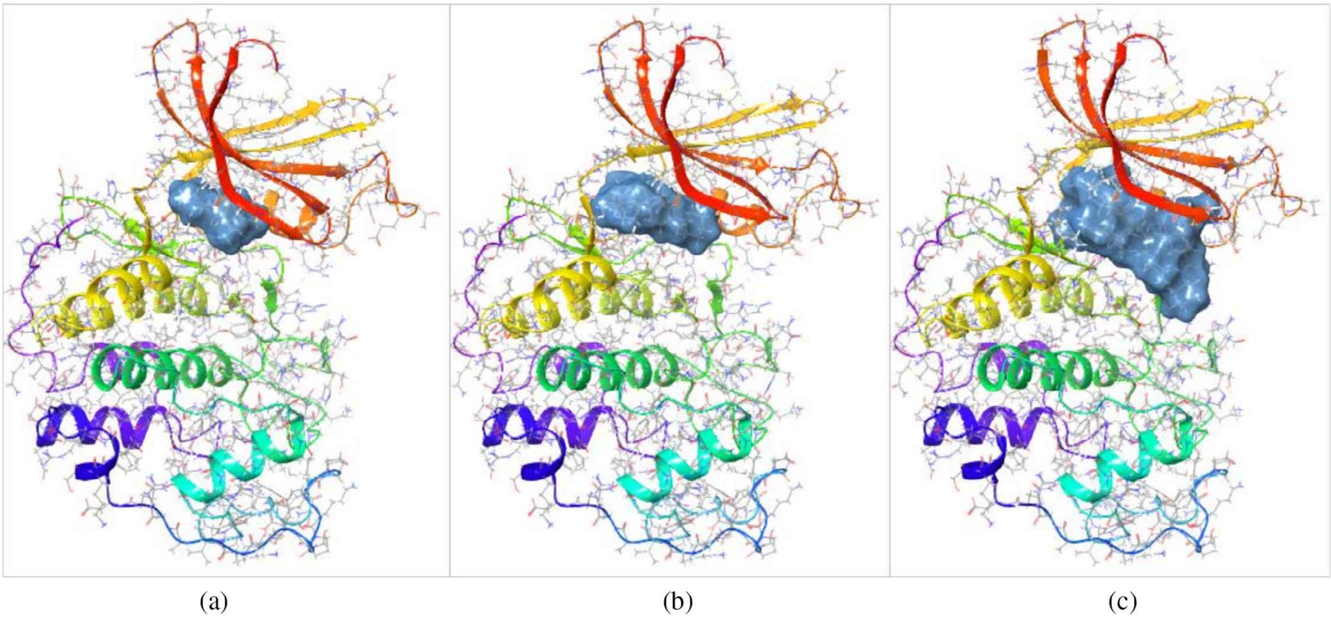
(a) (b) (c)

FIGURE 9 | Binding pocket representations of the 6GUB protein in complex with different compounds. (a) 6GUB–comp1, (b) 6GUB–comp2, and (c) 6GUB–comp3.

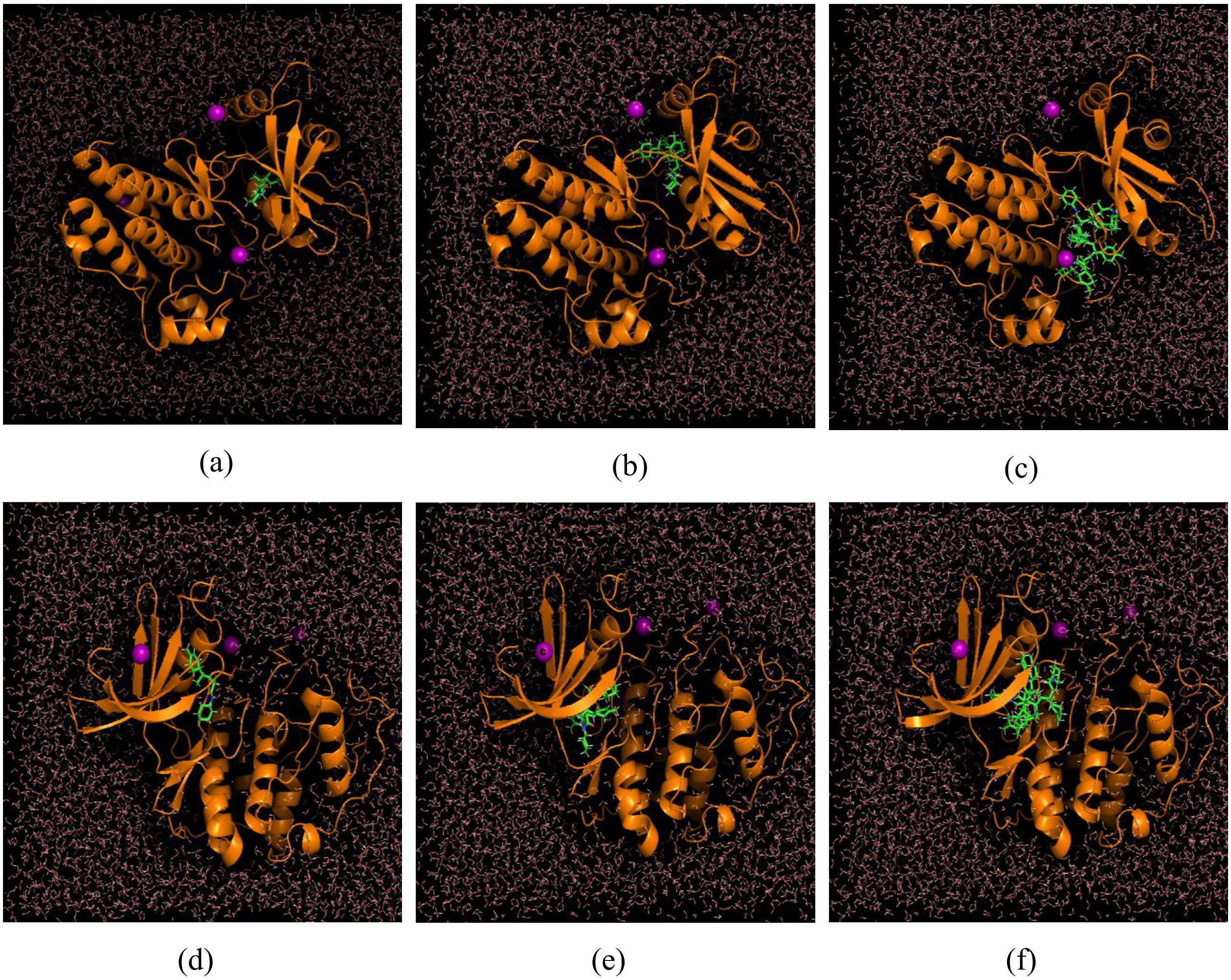
(a) (b) (c)

(d) (e) (f)

FIGURE 10 | The systems (a) comp1–3faa, (b) comp2–3faa, (c) comp3–3faa, (d) comp1–6gub, (e) comp2–6gub, and (f) comp1–6gub systems filled with water, neutralized with Cl⁻ (purple) ion.

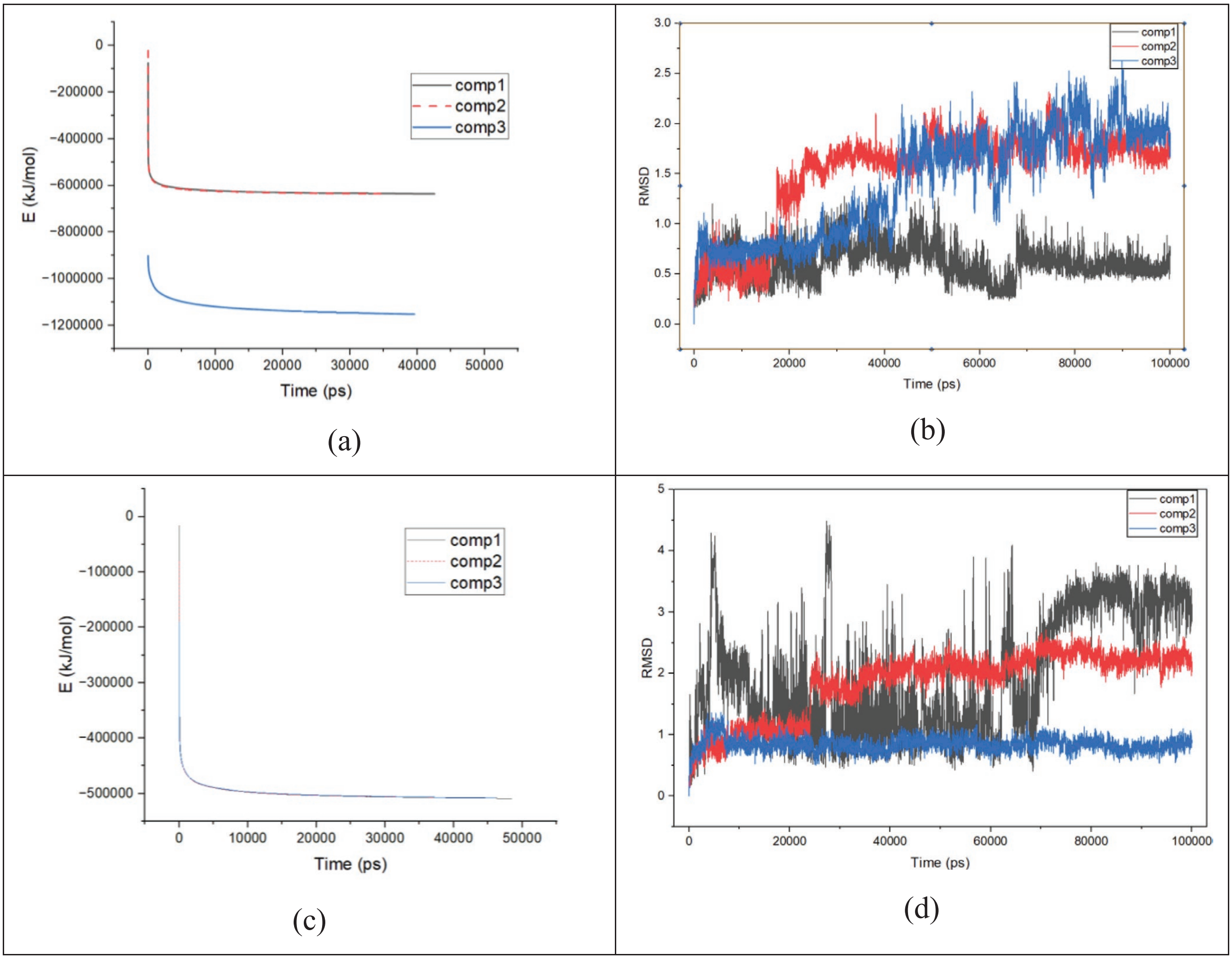

FIGURE 11 | (a) Total potential energy fluctuations, (b) root mean square deviation (RMSD) of 3faa–ligand system, (c) total potential energy fluctuations, and (d) root mean square deviation (RMSD) of 6gub–ligand system.

a steady state. However, significant differences were noted in the initial potential energy levels, equilibration times, and final energy values.

The potential energy profiles of the six ligand–receptor complexes were monitored throughout the 100 ns simulations (Figure 11a,c). In the 3FAA receptor, Comp1 and Comp2 exhibited similar mean potential energies of approximately -6.26×10^5 and -6.25×10^5 kJ/mol, respectively, with comparable fluctuations (standard deviations $\approx 1.6–1.7 \times 10^4$ kJ/mol). By contrast, Comp3–3FAA displayed a much lower average potential energy ($\approx -1.13 \times 10^6$ kJ/mol), accompanied by a higher degree of fluctuation (std $\approx 3.0 \times 10^4$ kJ/mol). This suggests that Comp3 induces stronger but also more dynamic interactions within the 3FAA pocket, whereas Comp1 and Comp2 remain in a narrower and more stable energy range.

For the 6GUB receptor, the three complexes maintained very similar potential energy levels ($\approx -5.00 \times 10^5$ kJ/mol). The fluctuations were lower than those observed in the 3FAA systems, with Comp3 showing the smallest standard deviation ($\approx 1.22 \times 10^4$ kJ/mol), indicating the most stable energy profile among the three, while Comp1 exhibited slightly larger variations.

A cross-receptor comparison highlights that the 3FAA systems, particularly Comp3, reached more negative potential energy values overall, reflecting stronger receptor–ligand interactions but also greater energetic variability. In contrast, the 6GUB systems were characterized by more compact energy distributions with reduced fluctuations, consistent with their more stable energetic behavior during the simulation.

For a more comprehensive assessment, further analyses of temperature, pressure, and root–mean–square deviation (RMSD) are essential to understanding the dynamic behavior of the systems. The RMSD analysis was performed to assess the structural stability and conformational dynamics of the ligand–receptor complexes over the 100 ns simulation period. The RMSD values provide insights into the extent of conformational fluctuations upon ligand binding and thus reflect the stability of the complexes in the solvated environment. The results for each system are illustrated in Figure 11b,d.

For the 3FAA–Comp1 complex, the average RMSD was calculated as 0.61 nm, with a maximum deviation of 1.33 nm. This relatively low fluctuation profile indicates that Comp1 binding to 3FAA leads to a stable complex with limited conformational drift throughout the simulation. In contrast, the 3FAA–Comp2 system exhibited a higher average RMSD of 1.50 nm, reaching up to 2.32 nm. The wider fluctuation range suggests that this complex is more conformationally flexible, reflecting structural adjustments during the simulation. Similarly, the 3FAA–Comp3 complex displayed an average RMSD of 1.41 nm, with maximum deviations of 2.63 nm. Although slightly more variable than Comp2, the overall trend indicates considerable conformational dynamics compared to Comp1. Collectively, among the 3FAA systems, Comp1 forms the most stable complex, whereas Comp2 and Comp3 exhibit greater structural flexibility.

In the 6GUB receptor systems, the complexes demonstrated distinct behavior. The 6GUB–Comp1 complex recorded the highest fluctuations, with an average RMSD of 1.96 nm and a maximum of 4.49 nm, suggesting significant conformational rearrangements and limited stability. The 6GUB–Comp2 system also showed elevated deviations, with an average RMSD of 1.84 nm and a maximum of 2.71 nm, reflecting a similarly unstable interaction profile. By contrast, the 6GUB–Comp3 complex exhibited markedly greater stability, with an average RMSD of only 0.84 nm and a maximum deviation of 1.37 nm. The consistently low fluctuation range highlights Comp3 as the most stable ligand within the 6GUB binding site.

When comparing both receptor systems, it becomes evident that the 3FAA complexes generally maintain lower RMSD values, indicating more stable conformational behavior than their 6GUB counterparts. An exception is the 6GUB–Comp3 system, which displayed outstanding stability and even surpassed the performance of Comp2 and Comp3 in 3FAA. Taken together, these findings emphasize that the stability of ligand binding is strongly receptor–dependent: 3FAA favors Comp1 through polar stabilization, while 6GUB demonstrates a clear preference for Comp3, whose balanced polar and hydrophobic interactions contribute to its enhanced structural stability during the simulation.

When the RMSD profiles are compared with the docking results, complementary trends emerge. In the 3FAA receptor, Comp1 exhibited the most favorable docking score (−9.9 kcal/mol) supported by directional hydrogen bonds, and this was consistent with its low average RMSD (0.61 nm), indicating that strong polar anchoring translated into structural stability during the simulation. In contrast, Comp2 and Comp3 displayed docking scores of −9.2 and −9.4 kcal/mol, respectively, yet their RMSD values were higher (1.50 and 1.41 nm), suggesting that although both ligands were predicted to bind strongly in docking, the complexes underwent more pronounced conformational fluctuations under dynamic conditions.

In the 6GUB receptor, Comp3 achieved the strongest docking affinity (−9.3 kcal/mol) and simultaneously showed the lowest RMSD value (0.84 nm), highlighting excellent agreement between static docking predictions and dynamic stability. Comp2, with a docking score of −8.8 kcal/mol, formed stabilizing hydrogen bonds with LYS142 and ASP145; however, its higher RMSD (1.84 nm) revealed that these interactions were insufficient to prevent conformational drift during the simulation. Comp1, consistent with its weakest docking score (−7.5 kcal/mol), also exhibited the largest fluctuations (1.96 nm), confirming limited compatibility with the 6GUB binding pocket.

Overall, the integration of docking and RMSD analyses underscores the receptor–dependent binding behavior of the ligands. For 3FAA, Comp1 emerges as the most reliable binder, combining high docking affinity with dynamic stability, whereas for 6GUB, Comp3 demonstrates the most consistent performance across both computational approaches. These results highlight the necessity of complementing docking predictions with long–timescale MD simulations to capture the full spectrum of ligand–receptor interaction stability.

Temperature monitoring was performed throughout the 100 ns MD simulations to evaluate the thermal stability of each ligand–receptor complex. The average temperatures of all systems remained close to the target value of 300 K, with only minor deviations, confirming that the thermostat maintained the systems under physiologically relevant conditions. The results are summarized in Figure 12.

For the 3FAA receptor systems, Comp1, Comp2, and Comp3 all exhibited average temperatures around 299.9–300.0 K with standard deviations of ~1.7 K. The minimum values were approximately 293 K, while the maximum ranged between 306 and 307 K. These small variations indicate that the 3FAA complexes were thermally well balanced, with negligible differences among the three ligands.

In the 6GUB receptor systems, the average temperatures were also ~300 K, with slightly higher fluctuations compared to 3FAA. Comp1 showed a minimum temperature of 291.6 K and a maximum of 307.3 K, while Comp2 and Comp3 reached up to 307.7 and 308.1 K, respectively. The standard deviations (~1.9 K) were marginally larger than those of the 3FAA complexes, reflecting slightly greater thermal variability, though still within acceptable stability limits.

When comparing the two receptor groups, the 3FAA complexes demonstrated marginally tighter thermal control, while the 6GUB complexes displayed slightly broader fluctuation ranges, particularly for Comp2 and Comp3. Nevertheless, all systems maintained thermal stability around the reference value of 300 K, confirming that the simulation conditions were well regulated and that no abnormal heating or cooling events occurred.

Pressure fluctuations were monitored across all six ligand–receptor complexes during the 100 ns simulations to assess system equilibration and stability under the NPT ensemble. The target reference pressure was maintained at 1 bar, yet MD simulations are inherently characterized by large instantaneous fluctuations due to finite system size and periodic boundary conditions. The statistical averages and deviations are summarized in Figure 13.

For the 3FAA receptor systems, average pressures were close to the reference value (Comp1: 1.20 bar, Comp2: −0.46 bar, Comp3: 3.26 bar). However, the standard deviations were large

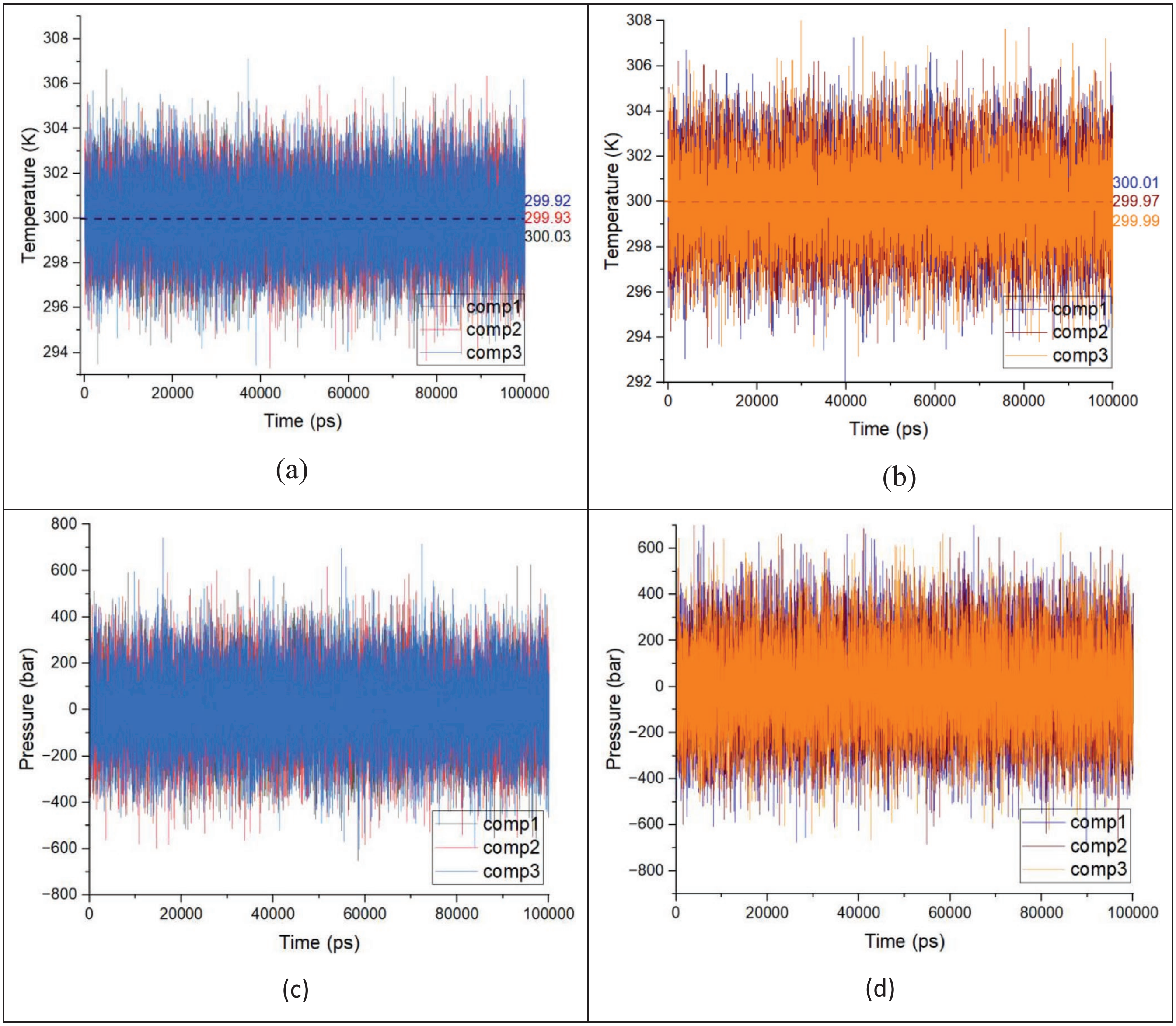

FIGURE 12 | Temporal fluctuations in temperature (K) over 10,000 ps for (a) 3faa–ligand system, (b) 6gub–ligand system temporal fluctuations in pressure (bar) over the same period, (c) 3faa–ligand system and (d) 6gub–ligand system.

(~164–167 bar), with minimum and maximum values ranging from approximately −650 to +740 bar. These wide ranges reflect the inherent compressibility of the system and the microscopic fluctuations typical of biomolecular simulations. Importantly, despite the magnitude of instantaneous variations, the mean values remained near the expected 1 bar reference, indicating proper pressure coupling.

In the 6GUB receptor systems, a similar pattern was observed. Average pressures were again near the reference (Comp1: 0.70 bar, Comp2: 2.48 bar, Comp3: 3.34 bar), while standard deviations were even larger (~189 bar). The pressure extrema reached between −684 and +750 bar across the different complexes. As with the 3FAA systems, these results highlight substantial fluctuations at short timescales but overall stable mean pressures consistent with the NPT simulation conditions.

When comparing both receptor groups, the 6GUB complexes exhibited slightly larger pressure deviations than the 3FAA systems, though both sets displayed broad fluctuation ranges. These findings are consistent with expectations for solvated protein–ligand systems of this size and do not indicate instabilities, as the pressure averages remained within acceptable proximity to the 1 bar reference.

Hydrogen bond (H bond) dynamics were quantified over the 100 ns trajectories to assess the persistence and multiplicity of ligand–receptor polar contacts. "Stability (%)" corresponds to $100 \times \langle N_{\text{H-bond}} \rangle$, such that values greater than 100% indicate more than one H bond per frame on average. "Average bond lifetime" was estimated from the mean run length of frames with at least one H bond, using a time resolution of 0.01 ns per step. Results are illustrated in Figure 8.

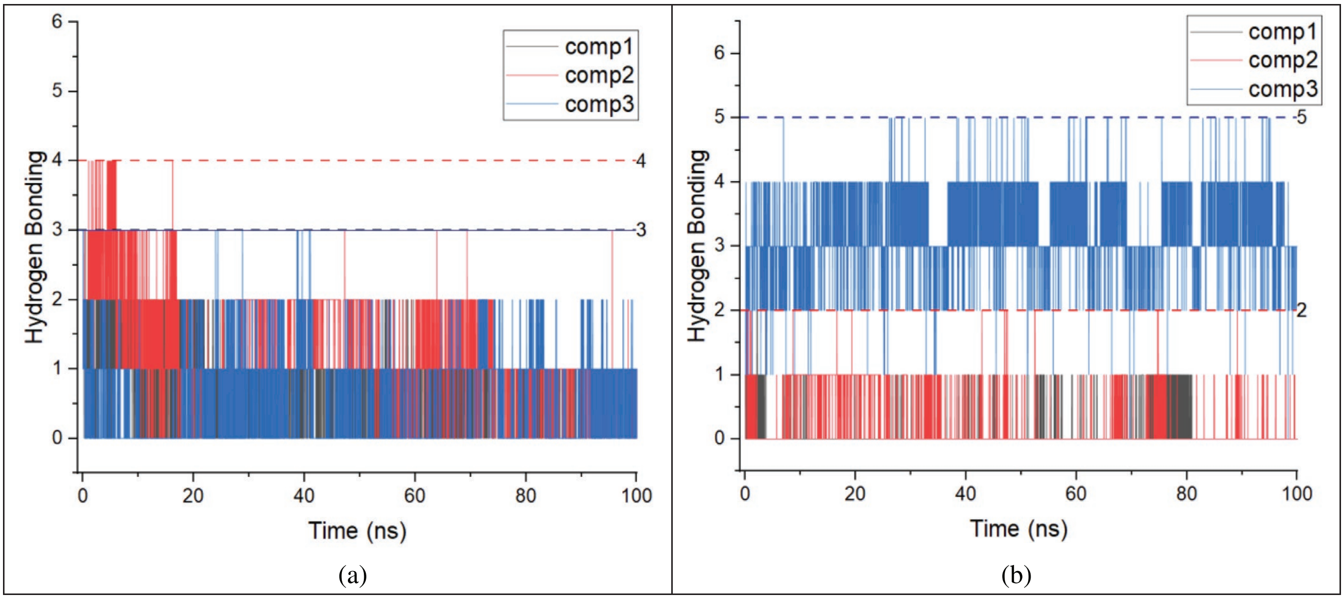

(a) (b)

FIGURE 13 | Hydrogen bonding number versus simulation time of (a) 3faa–ligand system and (b) 6gub–ligand system.

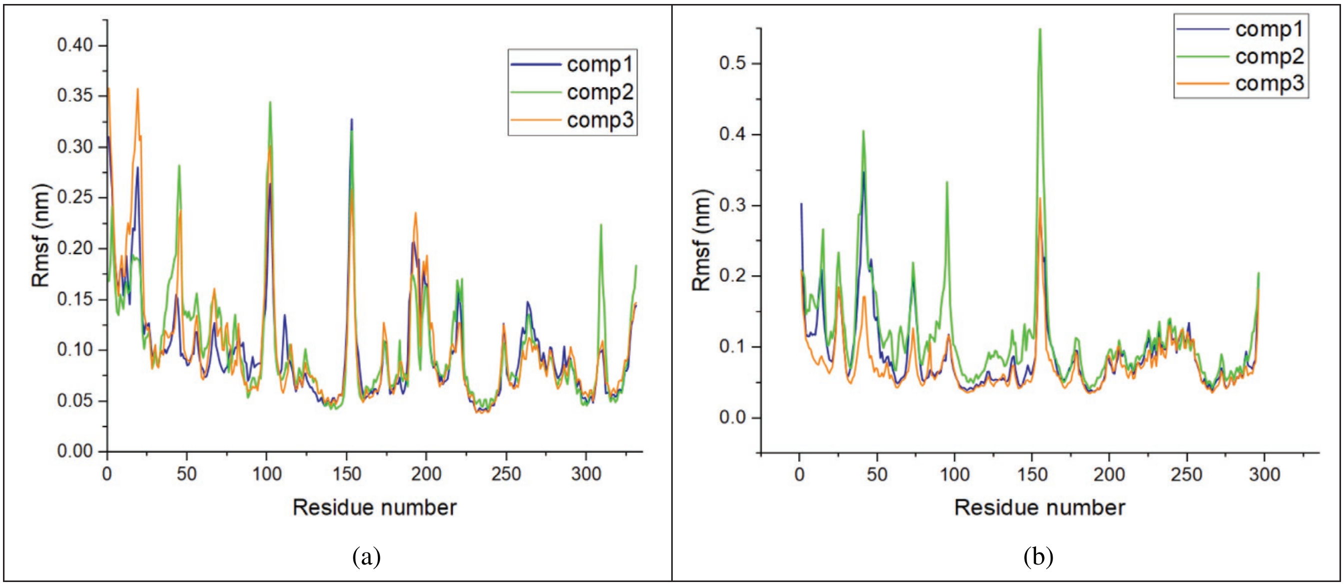

(a) (b)

FIGURE 14 | The plots show the fluctuation of binding energy per residue for (a) 3faa–ligand, (b) 6gub–ligand systems, with residue number on the *x*-axis and root mean square fluctuation (RMSF) in nm on the *y*-axis.

For the 3FAA receptor systems, Comp1 maintained an average of 0.87 hydrogen bonds per frame (stability 87.31%) with an average bond lifetime of 6.63 steps (~0.066 ns) and reached a maximum of three hydrogen bonds during the simulation. Comp2 formed on average 1.40 hydrogen bonds per frame (stability 139.54%) with a lifetime of 30.91 steps (~0.309 ns) and reached a maximum of four hydrogen bonds. Comp3 displayed the lowest H bonding capacity, averaging 0.51 bonds per frame (stability 51.13%) with a lifetime of 5.48 steps (~0.055 ns), with a maximum of three hydrogen bonds. The order of stability in the 3FAA receptor was therefore Comp2 > Comp1 > Comp3.

For the 6GUB receptor systems, Comp1 exhibited very weak hydrogen bonding, averaging only 0.08 bonds per frame (stability 7.74%) with a lifetime of 2.02 steps (~0.020 ns), and reached a maximum of two hydrogen bonds. Comp2 showed moderate binding, with 0.25 bonds per frame (stability 25.06%) and a lifetime of 5.94 steps (~0.059 ns), reaching up to two hydrogen bonds. By contrast, Comp3 formed an average of 3.39 bonds per frame (stability 339.13%) with a remarkably long lifetime of 3333 steps (~33.33 ns) and reached a maximum of five hydrogen bonds.

In cross-receptor comparison, the dominant polar stabilizer differed. In 3FAA, Comp2 exhibited the strongest hydrogen

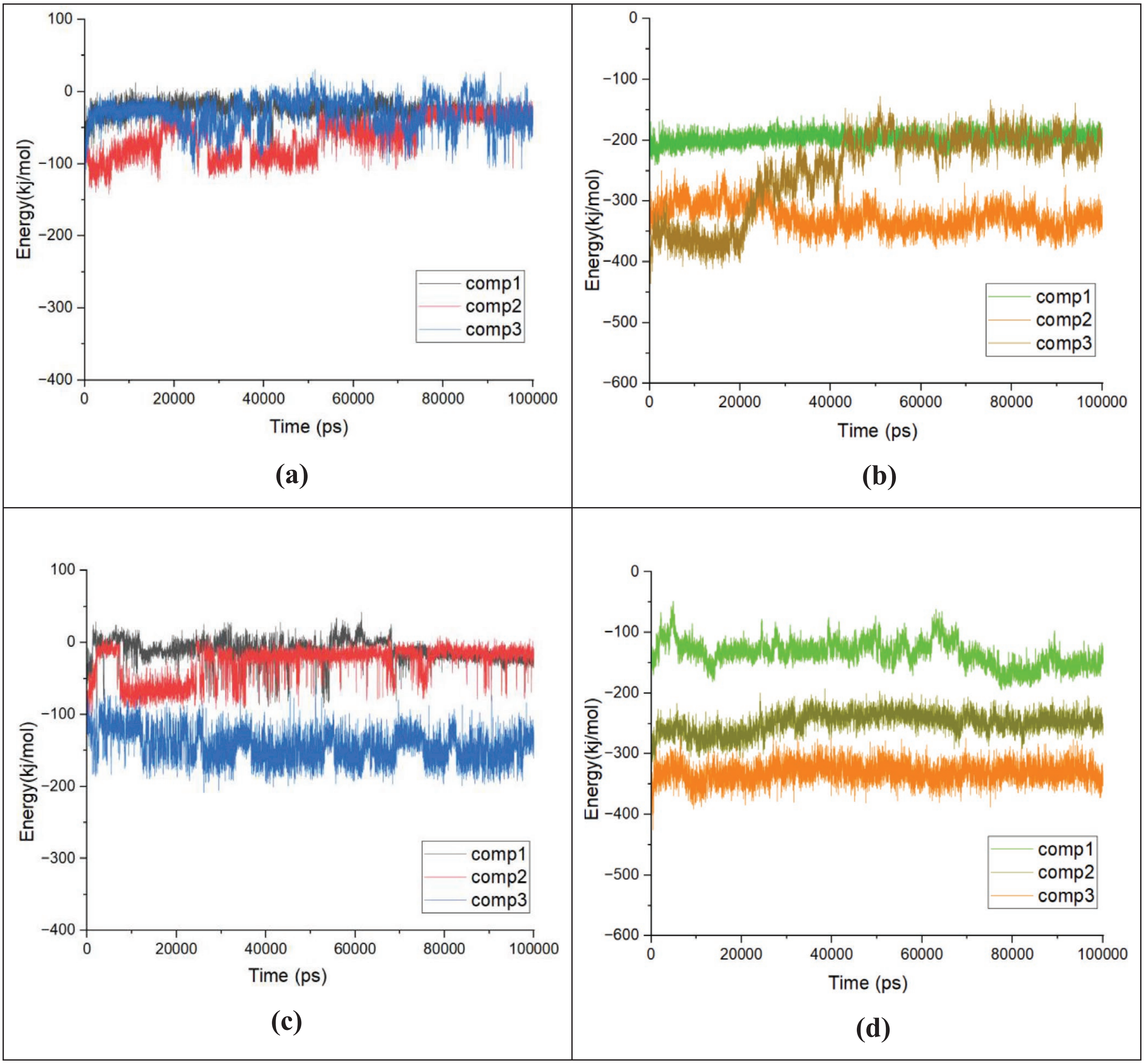

FIGURE 15 | Coulomb (Coul–SR) interaction energies between (a) 3faa–ligand system and (c) 6gub–ligand system. van der Waals (Lennard-Jones) interaction energies between (b) 3faa–ligand system and (d) 6gub–ligand system.

bonding interactions, while Comp1 was moderate and Comp3 relatively weak. In 6GUB, Comp3 clearly dominated, producing both the highest number and longest–lived hydrogen bonds, whereas Comp1 engaged in very few transient interactions. These results demonstrate that hydrogen bonding contributions are strongly receptor–dependent: 3FAA favors Comp2 through multiple persistent hydrogen bonds, while 6GUB strongly stabilizes Comp3 via a dense and long–lived hydrogen bond network.

Root mean square fluctuation (RMSF) analysis was performed to evaluate the flexibility of protein residues and the effect of ligand binding on local mobility. The RMSF values provide residue–level insights into conformational dynamics during the 100 ns simulations. The results are illustrated in Figure 14.

For the 3FAA receptor systems, Comp1 exhibited an average RMSF of 0.099 nm, with fluctuations ranging between 0.039 and 0.328 nm. Comp2 showed a comparable mean value of 0.103 nm (min 0.043 nm, max 0.345 nm), while Comp3 reached a similar average of 0.103 nm but extended to slightly higher maxima (0.358 nm). Overall, the three ligands induced similar flexibility patterns in 3FAA, with Comp1 showing marginally lower mean fluctuations and Comp3 displaying the broadest range.

In the 6GUB receptor systems, more pronounced differences were observed. Comp1 displayed an average RMSF of 0.091 nm (range 0.037–0.348 nm), while Comp2 showed the highest mobility with an average of 0.115 nm and a maximum of 0.556 nm, indicating localized regions of substantial flexibility. Comp3 demonstrated the lowest flexibility among the 6GUB complexes, with an average RMSF of 0.075 nm (range 0.035–0.311 nm).

Comparison within each receptor group highlights different stabilization patterns. In 3FAA, all three ligands induced similar flexibility with only minor differences, suggesting that binding did not drastically alter local residue mobility. In 6GUB, however, Comp3 provided the greatest structural stabilization, Comp1 maintained moderate flexibility, and Comp2 allowed the highest degree of residue fluctuations.

Cross–receptor comparison shows that 3FAA generally maintained balanced flexibility across all ligands, while 6GUB was more sensitive to ligand identity. Notably, Comp3–6GUB exhibited the lowest RMSF values across all systems, consistent with its strong hydrogen–bonding stability and low RMSD values, whereas Comp2–6GUB produced the highest residue fluctuations, reflecting weaker stabilization in this receptor context.

When considered alongside the hydrogen–bond and RMSD analyses, clear correlations emerge. Systems with more persistent hydrogen–bonding networks, such as 3FAA–Comp2 and 6GUB–Comp3, also exhibited reduced RMSF values, indicating that stable polar interactions contribute directly to minimizing receptor flexibility. Conversely, systems with fewer or transient hydrogen bonds, such as 6GUB–Comp2, showed greater fluctuations, reinforcing the link between hydrogen–bond stability, global conformational behavior, and local residue mobility.

An analysis of the temporal parameters in the interaction energy data presented in Figure 15 reveals that the interactions of Comp1, Comp2, and Comp3 ligands with the 3FAA and 6GUB receptors exhibit a dynamic profile. When Coulomb and van der Waals interactions were examined for the 3FAA receptor, the Comp1 complex showed an average electrostatic energy of approximately −25 kJ/mol and a van der Waals contribution of −197 kJ/mol, resulting in a total nonbonded energy of −222 kJ/mol. This indicates that the binding of Comp1 is primarily driven by hydrophobic contacts, with electrostatic stabilization playing a secondary role. In the Comp2–3FAA system, the Coulomb energy was −62 kJ/mol and the van der Waals contribution −326 kJ/mol, yielding a more favorable total of −388 kJ/mol. These results demonstrate that Comp2 achieves the most stable binding through a synergistic contribution of both electrostatics and hydrophobic interactions, which is consistent with its superior stability in the RMSD and hydrogen–bond analyses. The Comp3–3FAA complex exhibited a Coulomb energy of −30 kJ/mol and a van der Waals contribution of −249 kJ/mol, giving a total of −279 kJ/mol. This profile suggests that Comp3 interacts less favorably than Comp2, particularly in terms of electrostatics, leading to lower overall stability. Thus, within the 3FAA receptor, the energetic ranking is Comp2 > Comp3 > Comp1. In the 6GUB receptor, a different pattern emerged. The Comp1–6GUB complex presented a Coulomb contribution of −11 kJ/mol and a van der Waals energy of −134 kJ/mol, with a total nonbonded energy of −145 kJ/mol, representing the weakest binding among the three ligands. The Comp2–6GUB complex displayed stronger stabilization, with Coulomb and van der Waals values of −29 kJ/mol and −249 kJ/mol, respectively, leading to a total of −278 kJ/mol. Although stronger than Comp1, this interaction was still weaker than the corresponding 3FAA complex, showing that Comp2 is less efficient in the 6GUB binding site. The Comp3–6GUB system clearly stood out, with Coulomb interactions averaging −143 kJ/mol and van der Waals interactions −331 kJ/mol, producing a total of −474 kJ/mol. This exceptionally favorable stabilization matches the dense and long-lived hydrogen–bond network observed previously. The ranking within the 6GUB receptor is therefore Comp3 ≫ Comp2 > Comp1.

Considering both receptors together, it becomes evident that Comp2 is the strongest binder in 3FAA, while Comp3 is clearly dominant in 6GUB. These findings confirm that ligand binding efficiency is highly receptor–dependent: in 3FAA, Comp2 benefits from a balanced electrostatic–hydrophobic profile, whereas in 6GUB, Comp3 is favored by the synergistic contributions of highly negative Coulomb and van der Waals interactions.

3.6 | Residue-Level Decomposition and Binding Free Energy Analysis

The Molecular Mechanics Poisson–Boltzmann Surface Area (MMPBSA) method is a widely used approach for calculating ligand–receptor binding free energy by utilizing conformations obtained from MD simulations [24, 25]. In this method, the total binding energy (ΔG_{bind}) is derived by subtracting the free energies of the unbound receptor and ligand from the energy of the complex:

$$\Delta G_{\text{bind}} = G_{\text{complex}} - \left(G_{\text{receptor}} + Gl_{\text{igand}}\right)$$

here G_{complex} represents the total energy of the system when the ligand and receptor are bound together, while G_{receptor} and Gl_{igand} denote the free energies of the individual components. This energy is composed of the sum of the molecular mechanics energy (E_{MM}) and solvation energy ($G_{\text{solvation}}$):

$$G = E_{\text{MM}} + G_{\text{solvation}}$$

The molecular mechanics energy components consist of van der Waals (E_{vdW}) and electrostatic (E_{elec}) interactions:

$$E_{\text{MM}} = E_{\text{vdW}} + E_{\text{elec}}$$

The solvation energy includes both polar (G_{polar}) and nonpolar (G_{nonpolar}) contributions:

$$G_{\text{solvation}} = G_{\text{polar}} + G_{\text{nonpolar}}$$

Thus, the total binding energy can be expressed as:

$$\Delta G_{\text{bind}} = \left(E_{\text{vdW}} + E_{\text{elec}}\right) + \left(G_{\text{polar}} + G_{\text{nonpolar}}\right)$$

A more negative total binding energy (ΔG_{bind}) indicates a stronger ligand–receptor interaction, reflecting higher binding affinity. Notably, van der Waals forces and electrostatic interactions are known to play a crucial role in ligand binding [26].

Using the MMPBSA method, the binding energies of Comp1, Comp2, and Comp3 with the 3FAA and 6GUB receptors were analyzed. The evaluation was performed based on van der Waals energy, electrostatic energy, polar solvation energy, non-polar solvation energy, and total binding energy.

Per–residue free energy decomposition was performed to identify the contributions of individual receptor residues to the binding of Comp1, Comp2, and Comp3 with the 3FAA receptor. The energetic terms were separated into van der Waals, electrostatic, polar solvation, and non–polar solvation components, with the total binding free energy calculated for each residue. Negative

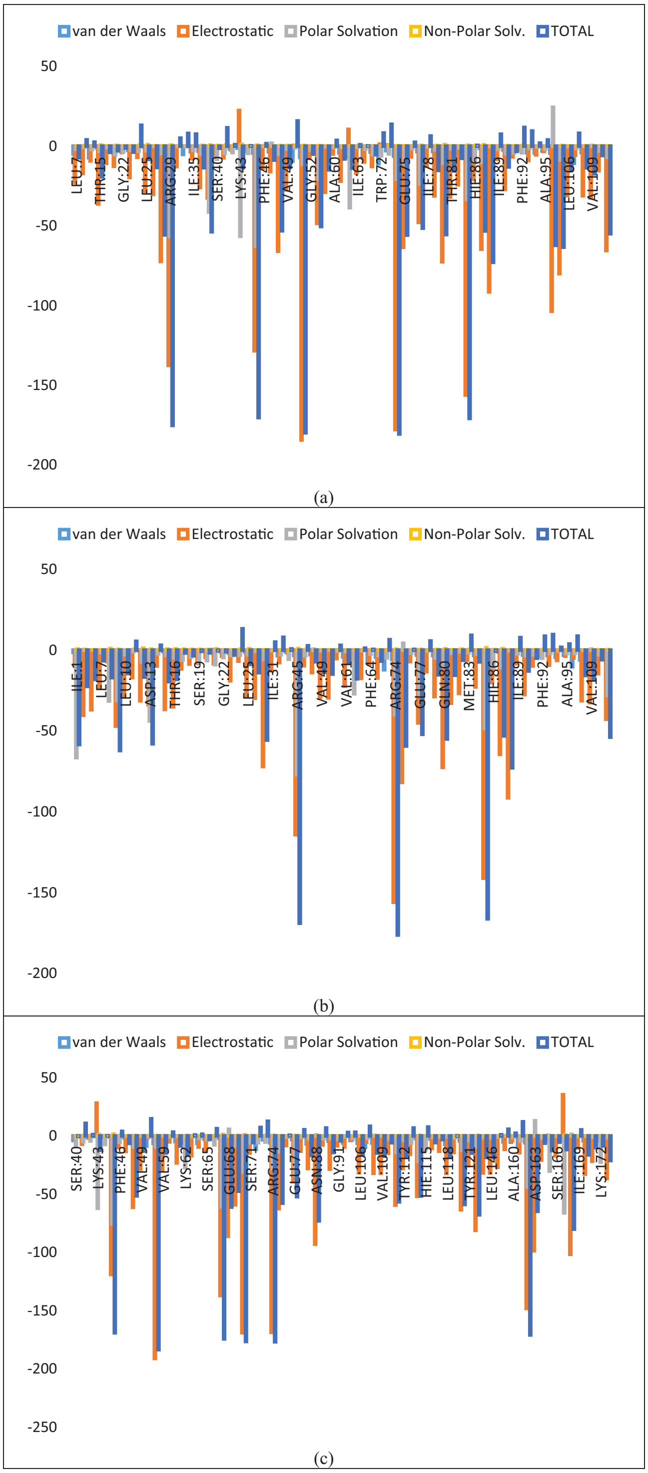

FIGURE 16 | Residue contribution energies **of** (a) 3faa–comp1, (b) 3faa–comp2, and (c) 3faa–comp3.

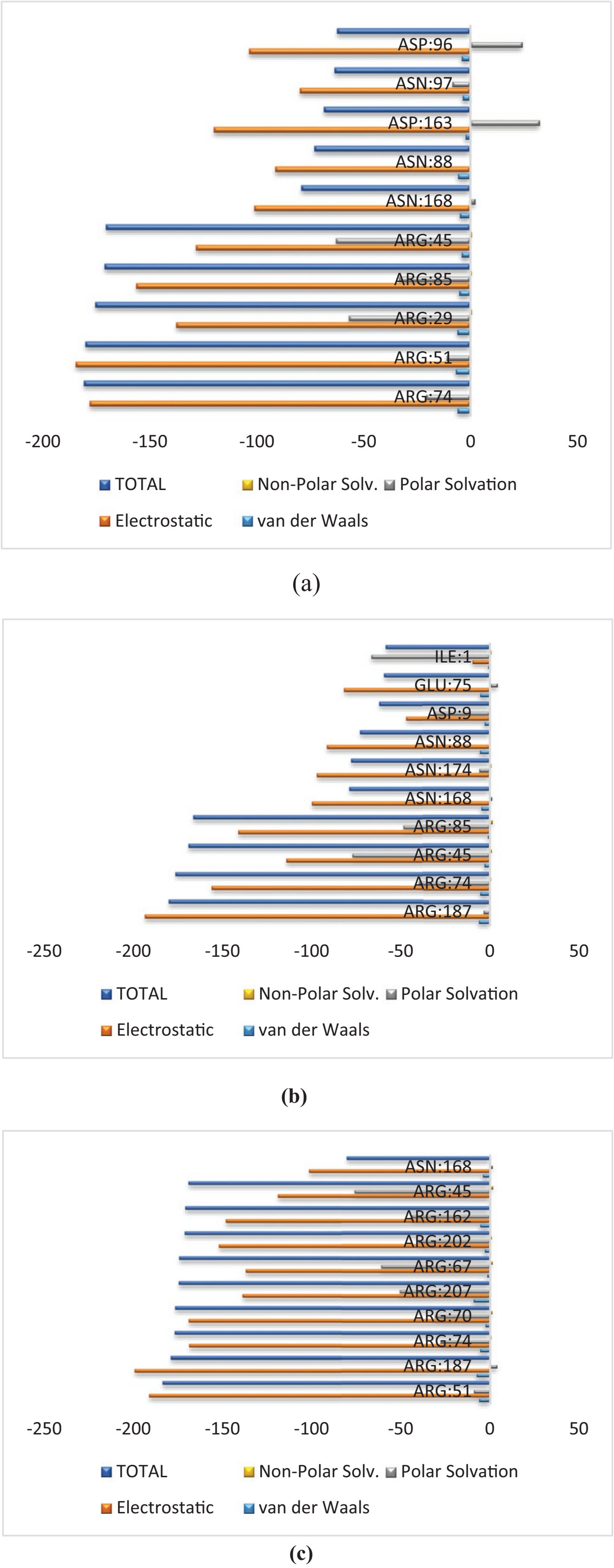

FIGURE 17 | Binding energy contributions of selected 10 residues for (a) 3faa–comp1, (b) 3faa–comp2, and (c) 3faa–comp3.

total values correspond to favorable stabilization, whereas positive values reflect unfavorable contributions. The overall decomposition profiles are presented in Figure 11, while the top 10 most favorable residues for each complex are highlighted in Figure 12.

The analysis revealed that all three ligands interact primarily with an arginine–rich region of the 3FAA binding pocket, where strong electrostatic stabilization dominates. In the Comp1–3FAA system, stabilization was driven by residues such as THR15, LEU7, MET14, and GLY20, with the most negative contributions arising from arginine residues including ARG74, ARG51, and ARG29. Additional contributions from ASN168, ASN88, and ASP163 further supported binding. This indicates that Comp1 relies on a limited number of strong electrostatic anchors complemented by moderate hydrophobic contacts.

The Comp2–3FAA complex exhibited the most favorable energetic profile. Strong binding contributions were distributed across multiple residues, particularly ILE1 and THR5, as well as arginine residues including ARG187, ARG74, ARG45, and ARG85. Polar residues such as ASN168 and ASN174 also contributed significantly. This widespread stabilization network confirms that Comp2 achieves the strongest binding among the three ligands through a synergistic balance of electrostatics and van der Waals forces.

For the Comp3–3FAA system, binding stabilization was provided by residues such as LYS43 and several arginine residues. The most favorable contributions came from ARG51, ARG187, ARG74, ARG70, and ARG207, with additional support from ARG67, ARG202, and ARG162 (Figures 16 and 17). While these residues form an extensive stabilizing cluster, the overall balance of solvation effects was less favorable compared to Comp2, leading to reduced net stability.

Taken together, the decomposition analysis and hotspot residue identification clearly demonstrate that Comp2 is the most favorable ligand in the 3FAA receptor, as it engages multiple residues with strong and coherent contributions, producing the lowest binding free energy. Comp1 shows moderate stabilization with fewer high-impact residues, while Comp3 relies on a wide distribution of arginine residues but with less favorable solvation balance. These results are fully consistent with the docking, RMSD, RMSF, and hydrogen bond analyses, reinforcing the conclusion that Comp2 exhibits the most stable and energetically favorable binding within the 3FAA receptor pocket.

In contrast to the 3FAA receptor, the per–residue decomposition of binding free energy in 6GUB highlighted a more extensive and cohesive network of stabilizing residues. The decomposition profiles are displayed in Figure 18, while the 10 residues with the most favorable contributions for each complex are presented in Figure 19.

For the Comp1–6GUB complex, binding stabilization was relatively limited and largely dependent on individual arginine residues. The strongest contributions originated from ARG36 (−175.6 kJ/mol) and ARG50 (−174.9 kJ/mol), while additional moderate support came from residues such as ASN132, ASP127, and GLN85. The overall pattern suggests that Comp1 engages only a narrow subset of residues, leaving large regions of the pocket underutilized.

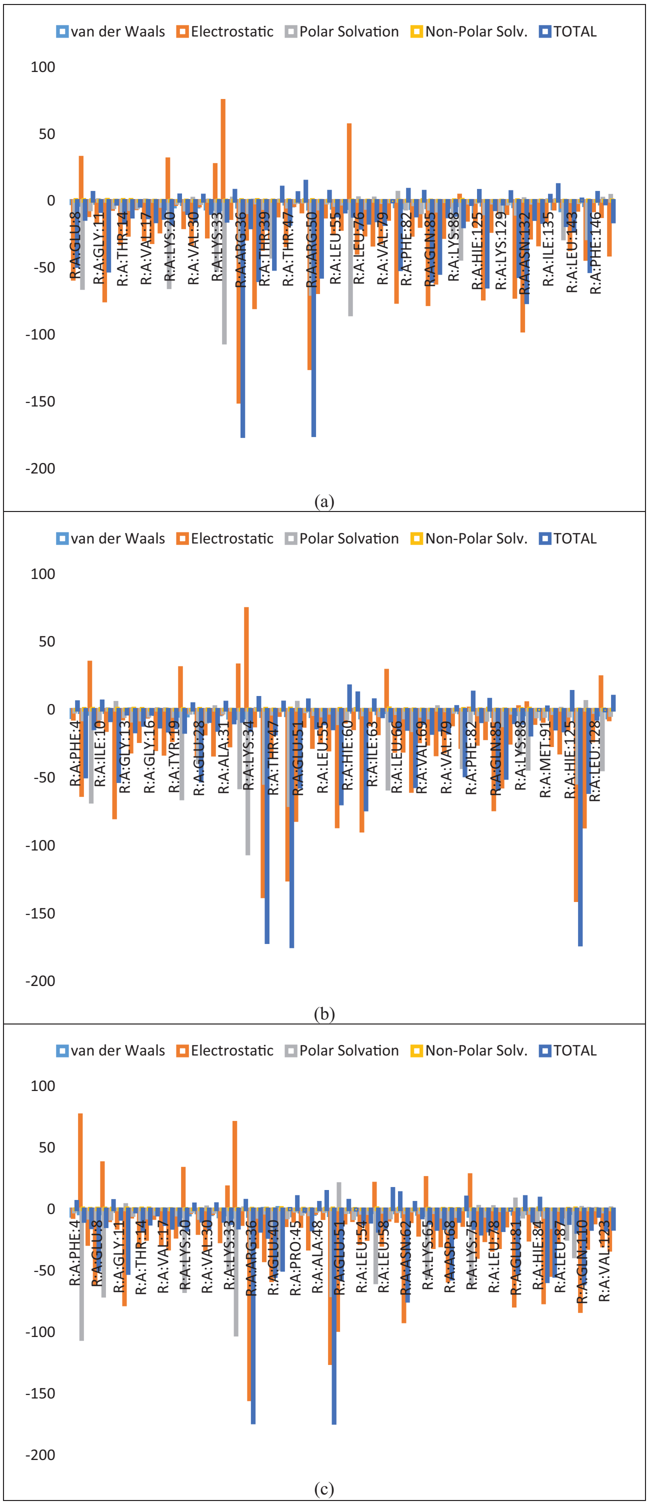

FIGURE 18 | Residue contribution energies of (a) 6gub–comp1, (b) 6gub–comp2, and (c) 6gub–comp3.

The Comp2–6GUB system exhibited a broader but still moderate distribution of stabilizing interactions. Major arginine residues

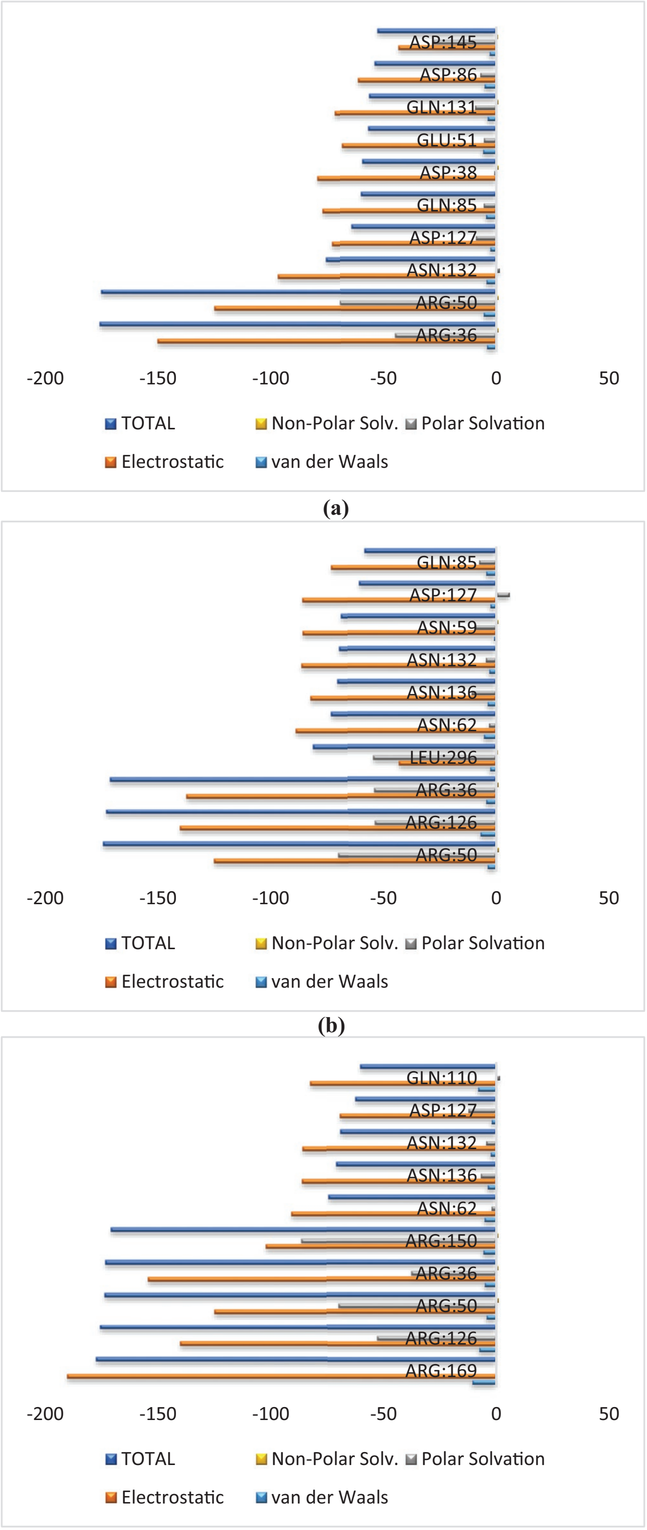

FIGURE 19 | Binding Energy Contributions of Selected 10 Residues for (a) 6gub–comp1, (b) 6gub–comp2, and (c) 6gub–comp3.

such as ARG50 (−174.2 kJ/mol), ARG126 (−172.9 kJ/mol), and ARG36 (−171.1 kJ/mol) dominated the profile, supplemented by contributions from LEU296, ASN62, and ASN136. Compared to Comp1, Comp2 involved a greater diversity of residues, combining both electrostatic and hydrophobic contacts, yet the magnitude of stabilization was less pronounced than that observed in Comp3.

The Comp3–6GUB complex displayed the most striking decomposition pattern. Multiple residues simultaneously provided highly favorable contributions, including ARG169 (−177.5 kJ/mol), ARG126 (−175.7 kJ/mol), ARG50 (−173.7 kJ/mol), ARG36 (−173.4 kJ/mol), and ARG150 (−170.9 kJ/mol). Additional polar residues such as ASN62 and ASN136 reinforced this network. The widespread distribution and consistently strong negative contributions indicate that Comp3 achieves a dense and persistent interaction network across the binding site, in line with its superior performance in global binding free energy, hydrogen bond persistence, and RMSD stability.

Overall, the 6GUB decomposition analysis underscores a receptor environment where Comp3 clearly dominates by mobilizing a broad cluster of arginine residues to achieve deep electrostatic stabilization. Comp2 interacts with a more limited set of residues, providing intermediate stabilization, while Comp1 engages only a few hotspots and thus represents the weakest binder in this receptor.

A cross–receptor comparison of the decomposition results reveals a clear receptor–dependent preference in ligand stabilization. In the 3FAA receptor, Comp2 emerged as the most favorable ligand, engaging multiple residues with strong and coherent contributions, including both arginine and polar residues, supported by balanced electrostatic and hydrophobic interactions. Comp1 showed moderate stabilization, whereas Comp3 relied on an extended but less efficient arginine network, resulting in lower overall stability. By contrast, in the 6GUB receptor, Comp3 was identified as the dominant binder, forming a dense and widely distributed interaction network across arginine residues such as ARG169, ARG126, ARG50, and ARG36, supplemented by polar residues including ASN62 and ASN136. This extensive electrostatic anchoring translated into the strongest overall stabilization observed among all systems. Comp2 displayed intermediate stabilization in 6GUB, while Comp1 consistently showed the weakest. Taken together, these findings demonstrate that while Comp2 is favored in the 3FAA pocket through balanced electrostatic and van der Waals contributions, Comp3 dominates in 6GUB by mobilizing an extensive arginine–rich network that provides highly persistent electrostatic stabilization.

This section complements the decomposition results by integrating the total binding free energies (ΔG_{bind}, kcal/mol) obtained from MMPBSA analysis. ΔG_{bind} includes van der Waals, electrostatic, polar, and nonpolar solvation contributions; more negative values indicate stronger binding affinity.

In the 3FAA receptor, ΔG_{bind} values clearly confirmed the superiority of Comp2. Comp2–3FAA (−68.9 kcal/mol) was markedly more favorable than Comp1–3FAA (−43.7 kcal/mol) and Comp3–3FAA (−41.0 kcal/mol), providing an energetic advantage of about 25–28 kcal/mol. This trend is consistent with decomposition data showing that Comp2 engages multiple stabilizing hotspots (ARG187, ARG74, ARG45/ARG85, ASN168/ASN174), forming a coherent electrostatic and van der Waals network. Comp1 achieved moderate stabilization through a smaller set of residues (−43.7 kcal/mol), while Comp3 remained weaker (−41.0 kcal/mol), in line with its less favorable solvation balance.

In the 6GUB receptor, the ranking was reversed. Comp3–6GUB exhibited the most favorable ΔG_{bind} (−72.5 kcal/mol), substantially more stable than Comp2–6GUB (−47.5 kcal/mol) and Comp1–6GUB (−25.5 kcal/mol). Comp3's dominance aligns with per-residue analysis, which highlighted its engagement with a broad arginine cluster (ARG169, ARG126, ARG50, ARG36, ARG150) and complementary polar residues (ASN62, ASN136). Comp2 maintained an intermediate profile (−47.5 kcal/mol), while Comp1 showed weak binding (−25.5 kcal/mol), reflecting limited stabilizing contacts.

Taken together, these results demonstrate a receptor-dependent binding preference. The 3FAA receptor strongly favors Comp2 due to its balanced electrostatic–hydrophobic contributions and multi-residue stabilization, whereas the 6GUB receptor preferentially stabilizes Comp3 through a dense arginine network and persistent polar anchoring. From a design perspective, this duality suggests two complementary strategies: enhancing balanced electrostatic–hydrophobic interactions for 3FAA-like binding pockets and maximizing multi-contact polar anchoring for 6GUB-like environments. These findings integrate well with RMSD/RMSF and hydrogen bond analyses, which also showed that Comp2 dominates in 3FAA and Comp3 in 6GUB, thereby validating the consistency across different levels of structural and energetic assessment.

4 | Conclusion

In this study, a copolymer of Limonene with N-Cyclohexylacrylamide (LIM-*co*-NCA) was successfully synthesized and characterized by FT-IR and ^{1}H-NMR spectroscopy techniques. The thermal properties of the copolymer LIM-*co*-NCA were detected by TGA/DTG, and the molecular weight of the copolymer LIM-*co*-NCA was determined by using GPC. As a result of the GPC analysis, it was determined that the synthesized limonene copolymers (LIM-*co*-NCA) had an oligomeric structure. It is known that the reactions of polymers cannot progress in 100% conversion, and the ability of limonene monomers to polymerize is quite low.

Extended 100 ns MD simulations combined with MMPBSA binding free energy analysis revealed clear receptor–dependent differences in the interactions of Comp1, Comp2, and Comp3 with their protein targets. Thermodynamic control parameters, including temperature and pressure, confirmed stable simulation conditions, ensuring that the observed trends arose from intrinsic ligand–receptor interactions. Structural analyses (RMSD and RMSF) indicated that Comp2 maintained the most stable binding profile in the 3FAA receptor, supported by persistent hydrogen bonds and balanced nonbonded interactions, whereas Comp3 achieved the most favorable stabilization in the 6GUB receptor through a dense, long–lived hydrogen–bond network and extensive electrostatic contributions.

Per–residue decomposition highlighted the structural determinants underlying these differences. In the 3FAA receptor, Comp2 engaged multiple hotspots including ARG187, ARG74, ARG45, ARG85, ASN168, and ASN174, producing a coherent network of electrostatic and van der Waals contacts. Comp1 relied on fewer but distinct residues such as THR15, LEU7, MET14, GLY20, ARG74, ARG51, and ARG29, whereas Comp3 drew stabilization from a broader but less favorable arginine cluster including ARG51, ARG187, ARG74, ARG70, and ARG207, together with LYS43 and additional arginine side chains. In the 6GUB receptor, Comp3 exploited an extensive arginine cluster—ARG169, ARG126, ARG50, ARG36, ARG150—supplemented by polar residues such as ASN62 and ASN136, creating a dense and persistent electrostatic network. Comp2 showed intermediate stabilization, relying on ARG50, ARG126, ARG36, LEU296, and ASN62, while Comp1 engaged a more limited set including ARG36, ARG50, ASN132, and ASP127.

Binding free energy calculations based on ΔG_{bind} values further reinforced this receptor-specific trend. In the 3FAA receptor, Comp2 exhibited the most favorable binding free energy ($\Delta G_{\mathrm{bind}} \approx -68.9$ kcal/mol), followed by Comp1 (≈ -43.7 kcal/mol) and Comp3 (≈ -41.0 kcal/mol), both of which were considerably weaker. In contrast, in the 6GUB receptor, Comp3 dominated with $\Delta G_{\mathrm{bind}} \approx -72.5$ kcal/mol, while Comp2 displayed intermediate stabilization (≈ -47.5 kcal/mol) and Comp1 remained the weakest binder (≈ -25.5 kcal/mol). Taken together, these findings highlight a receptor-dependent binding preference: Comp2 is the dominant ligand in 3FAA, whereas Comp3 is strongly favored in 6GUB. This outcome underscores that ligand binding performance is critically determined by the electrostatic and structural features of the receptor binding pocket, and the identification of key stabilizing residues provides valuable molecular-level guidance for the rational design of ligands optimized for specific receptor environments.

Conflicts of Interest

The authors declare no conflicts of interest.

Data Availability Statement

The data that support the findings of this study are available from the corresponding author upon reasonable request.

References

1. N. Sanshita Devi, B. Bhattacharya, A. Sharma, I. Singh, P. Kumar, and T. Sangnim, "From Citrus to Clinic: Limonene's Journey Through Preclinical Research, Clinical Trials, and Formulation Innovations," *International Journal of Nanomedicine* 20 (2025): 4433–4460.

2. P. Anandakumar, S. Kamaraj, and M. K. Vanitha, "D-Limonene: A Multifunctional Compound With Potent Therapeutic Effects," *Journal of Food Biochemistry* 45, no. 1 (2021): e13566.

3. E. S. Shalaby, S. I. Shalaby, and S. A. Ismail, "Advantages and Therapeutic Applications of Different Semisolids as Vehicles for Nano-Based Systems," *Therapeutic Delivery* 16, no. 6 (2025): 581–591.

4. D. Das, A. Singh, R. Adari, G. Mudgal, and P. Radha, "Biocompatible Cellulose Derivatives: Green Chemistry and Its Sustainable Applications," in *Functionalized Cellulose Materials: Sustainable Manufacturing and Applications* (Springer Nature Switzerland, 2025), 159–190.

5. M. Soni, M. K. Jha, U. Banjare, et al., "Aromatherapy in Combating Human Pathogens and Diseases: Impact and Prospects," *Journal of Essential Oil Bearing Plants* 28, no. 3 (2025): 1–470.

6. A. A. A. Alghamdi, "D-Limonene Exhibits Antiproliferative Activity Against Human Colorectal Adenocarcinoma (Caco-2) Cells via Regulation of Inflammatory and Apoptotic Pathways," *Current Issues in Molecular Biology* 47, no. 5 (2025): 370, https://doi.org/10.3390/cimb47050370.

7. B. M. Sahoo, B. K. Banik, S. Sharma, and B. Singh, "Current Insights Into Therapeutic Potential of Terpenoids as Anticancer Agents," *Anti-Cancer Agents in Medicinal Chemistry* 25, no. 5 (2025): 339–356.

8. F. Obermeier and O. I. Strube, "Limonene as Biobased Building Block for Functional Monoterpene Acrylate Monomers," *Journal of Coating Technology and Research* 22 (2025): 1223–1235, https://doi.org/10.1007/s11998-024-01031-1.

9. F. S. G. Valookolaei, H. Sazegar, and L. Rouhi, "Limonene Encapsulated Alginate/Collagen as Antibiofilm Drug Against *Acinetobacter Baumannii*," *BMC Biotechnology* 24 (2024): 86, https://doi.org/10.1186/s12896-024-00888-9.

10. K. K. Abla, S. Domiati, R. El Majzoub, and M. M. Mehanna, "Propranolol-Loaded Limonene-Based Microemulsion Thermo-Responsive Mucoadhesive Nasal Nanogel: Design, in Vitro Assessment, Ex Vivo Permeation, and Brain Biodistribution," *Gels* 9, no. 6 (2023): 491, https://doi.org/10.3390/gels9060491.

11. N. Çankaya, "Synthesis of Graft Copolymers Onto Starch and Its Semiconducting Properties," *Results in Physics* 6 (2016): 538–542.

12. N. Cankaya and M. M. Temüz, "Monomer Reactivity Ratios of Cellulose Grafted With N-Cyclohexylacrylamide and Methyl Methacrylate by Atom Transfer Radical Polymerization," *Cellulose Chemistry and Technology* 48, no. 3–4 (2014): 209–215.

13. N. Çankaya, E. Tanış, H. Elmalı Gülbaş, and N. Bulut, "A New Synthesize of Limonene Copolymer: Experimental and Theoretical Analysis," *Polymer Bulletin* 76, no. 7 (2019): 3297–3327, https://doi.org/10.1007/s00289-018-2543-3.

14. M. J. Frisch, G. W. Trucks, H. B. Schlegel, et al., *Gaussian 09, Revision A.02* (Gaussian, Inc, 2009).

15. A. D. Becke, "Density-Functional Thermochemistry. III. The Role of Exact Exchange," *Journal of Chemical Physics* 98, no. 7 (1993): 5648–5652.

16. A. E. Frisch and J. B. Foresman, *Exploring Chemistry With Electronic Structure Methods* (Gaussian Inc, 1996).

17. O. Trott and A. J. Olson, "AutoDock Vina: Improving the Speed and Accuracy of Docking With a New Scoring Function, Efficient Optimization and Multithreading," *Journal of Computational Chemistry* 31 (2010): 455–461.

18. M. J. Abraham, T. Murtola, R. Schulz, et al., "GROMACS: High Performance Molecular Simulations Through Multi-Level Parallelism From Laptops to Supercomputers," *Softwarex* 1 (2015): 19–25.

19. M. S. Valdés-Tresanco, M. E. Valdés–Tresanco, P. A. Valiente, and E. Moreno, "gmx_MMPBSA: A New Tool to Perform End–State Free Energy Calculations With GROMACS," *Journal of Chemical Theory and Computation* 17, no. 10 (2021): 6281–6291.

20. H. J. C. Berendsen, D. van der Spoel, and R. van Drunen, "GROMACS: A Message-Passing Parallel Molecular Dynamics Implementation," *Computer Physics Communications* 91, no. 1–3 (1995): 43–56.

21. D. E. Shaw Research, "Anton 2: Raising the Bar for Performance and Precision in Molecular Dynamics Simulation," *Science* 370, no. 6512 (2020): 1148–1154.

22. B. Hess, H. Bekker, H. J. C. Berendsen, and J. G. E. M. Fraaije, "LINCS: A Linear Constraint Solver for Molecular Simulations," *Journal of Computational Chemistry* 18, no. 12 (1997): 1463–1472.

23. M. Karplus and J. A. McCammon, "Molecular Dynamics Simulations of Biomolecules," *Nature Structural Biology* 9, no. 9 (2002): 646–652.

24. P. A. Kollman, I. Massova, C. Reyes, et al., "Calculating Structures and Free Energies of Complex Molecules: Combining Molecular Mechanics and Continuum Models," *Accounts of Chemical Research* 33, no. 12 (2000): 889–897.

25. N. Homeyer and H. Gohlke, "Free Energy Calculations by the Molecular Mechanics Poisson-Boltzmann Surface Area Method," *Molecular Informatics* 31, no. 2 (2012): 114–122.

26. S. Genheden and U. Ryde, "The MM/PBSA and MM/GBSA Methods to Estimate Ligand-Binding Affinities," *Expert Opinion on Drug Discovery* 10, no. 5 (2015): 449–461.